

2016

Seamless cross-scale modeling with SCHISM

Yinglong J. Zhang
Virginia Institute of Marine Science

F Ye
Virginia Institute of Marine Science

EV Stanev

S Grashorn

Follow this and additional works at: <https://scholarworks.wm.edu/vimsarticles>



Part of the [Aquaculture and Fisheries Commons](#)

Recommended Citation

Zhang, Yinglong J.; Ye, F; Stanev, EV; and Grashorn, S, "Seamless cross-scale modeling with SCHISM" (2016). *VIMS Articles*. 802.

<https://scholarworks.wm.edu/vimsarticles/802>

This Article is brought to you for free and open access by the Virginia Institute of Marine Science at W&M ScholarWorks. It has been accepted for inclusion in VIMS Articles by an authorized administrator of W&M ScholarWorks. For more information, please contact scholarworks@wm.edu.

1 **Seamless cross-scale modelling with SCHISM**

2

3 **Yinglong J. Zhang^{a1}, Fei Ye^a, Emil V. Stanev^b, and Sebastian Grashorn^b**

4 **a.** Virginia Institute of Marine Science,

5 College of William & Mary,

6 Center for Coastal Resource Management,

7 1375 Greate Road,

8 Gloucester Point, VA 23062,

9 USA

10 **b.** Helmholtz-Zentrum Geesthacht,

11 Max-Planck-Straße 1,

12 21502 Geesthacht,

13 Germany

14

15

16

¹ Corresponding author; e-mail: yjzhang@vims.edu; phone: (804) 684-7466; fax: (804) 684-7179.

17
18 **Abstract**
19 We present a new 3D unstructured-grid model (SCHISM) which is an upgrade from an existing model (SELFÉ).
20 The new advection scheme for the momentum equation includes an iterative smoother to reduce excess mass
21 produced by higher-order kriging method, and a new viscosity formulation is shown to work robustly for generic
22 unstructured grids and effectively filter out spurious modes without introducing excessive dissipation. A new higher-
23 order implicit advection scheme for transport (TVD²) is proposed to effectively handle a wide range of Courant
24 numbers as commonly found in typical cross-scale applications. The addition of quadrangular elements into the
25 model, together with a recently proposed, highly flexible vertical grid system (Zhang et al. 2015), leads to model
26 polymorphism that unifies 1D/2DH/2DV/3D cells in a single model grid. Results from several test cases
27 demonstrate the model's good performance in the eddying regime, which presents greater challenges for
28 unstructured-grid models and represents the last missing link for our cross-scale model. The model can thus be used
29 to simulate cross-scale processes in a seamless fashion (i.e. from deep ocean into shallow depths).

30
31 **Key words:** SCHISM; eddying regime; baroclinic instability; general circulation; Black Sea

32 33 **1 Introduction**

34 For the past two decades, great progress has been made in the application of unstructured-grid (UG) models to
35 coastal ocean processes. The superior boundary fitting and local refinement/derefinement ability of UG models
36 make them ideally suited for nearshore applications involving complex geometry and bathymetry. In particular, the
37 authors have previously demonstrated the great utility of UG models based on implicit time stepping schemes as the
38 latter effectively bypass the stringent CFL constraint and thus removes one of the most severe restrictions in UG
39 models (Zhang and Baptista 2008, hereafter ZB08); other time stepping methods such as predictor-corrector method
40 have also been proposed with somewhat stricter time step limit than ours (but more relaxed than the explicit mode-
41 splitting models) (Danilov 2012). The implicit UG models are free of mode-splitting errors and of the associated
42 filter to prevent modes aliasing.

43 Despite the great success of implicit UG models for barotropic problems (e.g., tides, storm surge and tsunami
44 inundations etc; Zhang et al. 2011, Bertin et al. 2014), their success for baroclinic problems remains modest so far
45 due to some unique challenges in such applications (e.g. pressure-gradient errors, diapycnal mixing etc), which
46 warrants further research effort. In fact, the success of UG models in the eddying regime has been very limited so far
47 compared to their structured-grid counterpart, and one of the reasons is that the larger velocity space compared to
48 the elevation space in UG models results in stronger spurious inertial modes that must be carefully controlled (Le
49 Roux 2005; Ringler et al. 2010; Danilov 2012). Note that the spurious modes appear in all models (structured or
50 unstructured), and can be excited from a variety of perturbation sources (Cotter and Ham 2011; Le Roux 2012), but
51 they are particularly severe in larger depths and along steep slopes.

52 We have been systematically improving the baroclinic capability of our UG model, and this paper serves as a
53 summary of the progress we have made in this endeavor for the past 5 years. Our experience suggests that for an UG
54 model to work well in the baroclinic regimes from shallow to large depths, it has to strike a careful balance between
55 accuracy, efficiency and robustness. For instance, the eddying regime sets a high standard for numerical dissipation
56 and stability (control of modes), whereas the order of numerical schemes is less important in the estuarine
57 applications, as the strong forcing therein favors stable and often lower-order numerical schemes. For such
58 applications, more emphasis should be placed on faithfully resolving geometric and bathymetric features that act as
59 the 1st-order forcing for the underlying processes. The rich diversity of the processes as found from shallow to large
60 depths likely precludes a 'one-size-fits-all' approach, and different numerical options may prove to be useful in
61 different regimes. This has been the guiding principle when we built our cross-scale model.

62 As far as the model (SELFÉ) we have been developing for the past 15 years is concerned, we have made steady
63 progress in the baroclinic regime in the *shallows* (ZB08; Burla 2010). Although all implicit models have inherent
64 numerical diffusion, SELFÉ seems to have struck a good balance between numerical dissipation (due to implicit
65 time stepping), numerical dispersion (due to Finite Element Method), and stability demanded by such type of
66 applications. However, the following areas need to be improved before it can become a bona fide cross-scale model.
67 First, the stratification is often under-estimated. This is related to the transport scheme as well as the vertical grid

68 system used (which is a hybrid system with part terrain-following S coordinates and part Z coordinates). The
69 situation improves significantly with the introduction of TVD scheme for transport, and recently a flexible LSC²
70 vertical grid (Zhang et al. 2015). Second, the model has not been applied in the eddying regime, which represents
71 the last missing link for a truly cross-scale model. One of the main focuses of this paper is on improving the model
72 in the eddying regime.

73 We have been working on a derivative product of the original SELFE model (v3.1dc;
74 http://www.stccmop.org/knowledge_transfer/software/selfe; last accessed Sept. 17, 2015), mostly due to license
75 disputes. However, the renaming of the model is probably long overdue as many important differences have
76 emerged between our branch of SELFE and the original SELFE for the past 3 years. The new model, SCHISM
77 (Semi-implicit Cross-scale Hydroscience Integrated System Model; www.schism.wiki, last accessed Sept. 17, 2015)
78 is being distributed with an open-source Apache v2 license, and has been operationally tested by Central Weather
79 Bureau of Taiwan (http://www.cwb.gov.tw/V7e/forecast/nwp/marine_forecast.htm; last accessed Sept. 17, 2015),
80 California Department of Water Resource
81 (http://baydeltaoffice.water.ca.gov/modeling/deltamodeling/models/bay_delta_schism/; last accessed Sept. 17,
82 2015), and National Laboratory of Civil Engineering, Portugal (LNEC; <http://ariel.lnec.pt/node/40>; last accessed
83 Sept. 17, 2015). Although the original focus of SCHISM is the same as SELFE, i.e., hydrodynamic applications, it
84 has since evolved into a comprehensive modeling framework (Fig. 1), courtesy of other developers and user groups
85 (<http://ccrm.vims.edu/schism/team.html>, last accessed Sept. 17, 2015). At the moment the SCHISM modelling
86 system includes: a wind-wave model (Roland et al 2012), 3 sediment transport models (Community Sediment
87 Transport Model (Pinto et al. 2012), SED2D (Dodet 2013), and TIMOR (Zanke 2003)), 2 biological/ecological
88 models (EcoSIM (Rodrigues et al. 2009) and CoSiNE, (Chai et al. 2002)), 2 oil spill models (Azevedo et al. 2014),
89 an age tracer model based on the work of Shen and Haas (2004), a generic tracer model, and a water quality model
90 (CE-QUAL-ICM, Cerco and Cole 1993). All modelling components have been parallelized using domain
91 decomposition MPI with generally good scalability.

92 For clarity, we list out the main new features of SCHISM as compared to SELFE v3.1dc:

- 93 1) Vertical grid system (LSC², Zhang et al. 2015);
- 94 2) Mixed triangular-quadrangular horizontal grid;
- 95 3) Implicit advection scheme for transport (TVD²);
- 96 4) Advection scheme for momentum: optional higher-order kriging with ELAD filter;
- 97 5) A new horizontal viscosity scheme (including bi-harmonic viscosity) to effectively filter out inertial spurious
98 modes without introducing excessive dissipation.

99 The 1st feature has been reported in Zhang et al. (2015), and the rest will be the subject of this paper.

100 To prepare for the introduction of the new SCHISM features, we will first briefly review some key formulations in
101 SELFE in Section 2, with the focus on the treatment of momentum advection. We then present the main differences
102 and new developments of SCHISM in Section 3, including the new advection schemes for momentum and transport
103 equations, and a filter-like bi-harmonic viscosity. Section 4 shows the extension of the formulations to mixed
104 triangular-quadrangular grids. Several challenging test cases are presented in Section 5 to benchmark the model in
105 the eddying regime. Together with previously demonstrated model capability in the non-eddy regimes, the new
106 capability in the eddying regime brings forth a seamless cross-scale model that is equally skillful from shallow to
107 deep oceans. Section 6 concludes the paper.

108

109 2. SELFE formulation

110 To clearly show the new revisions in SCHISM, in this section we briefly review some key formulations in SELFE
111 v3.1dc (ZB08). SELFE solves the Reynolds-averaged Navier-Stokes equation in its hydrostatic form and transport
112 of salt and heat:

113 Momentum equation:
$$\frac{D\mathbf{u}}{Dt} = \frac{\partial}{\partial z} \left(\nu \frac{\partial \mathbf{u}}{\partial z} \right) - g \nabla \eta + \mathbf{F}, \quad (1)$$

114 Continuity equation in 3D and 2D depth-integrated forms:

115 $\nabla \cdot \mathbf{u} + \frac{\partial w}{\partial z} = 0,$ (2)

116 $\frac{\partial \eta}{\partial t} + \nabla \cdot \int_{-h}^{\eta} \mathbf{u} dz = 0,$ (3)

117 Transport equations:

118 $\frac{\partial C}{\partial t} + \nabla \cdot (\mathbf{u}C) = \frac{\partial}{\partial z} \left(\kappa \frac{\partial C}{\partial z} \right) + F_h,$ (4)

119 where

120 $\nabla \left(\frac{\partial}{\partial x}, \frac{\partial}{\partial y} \right)$

121 D/Dt material derivative

122 (x,y) horizontal Cartesian coordinates

123 z vertical coordinate, positive upward

124 t time

125 $\eta(x, y, t)$ free-surface elevation

126 $h(x, y)$ bathymetric depth

127 $\mathbf{u}(x, y, z, t)$ horizontal velocity, with Cartesian components (u, v)

128 w vertical velocity

129 \mathbf{F} other forcing terms in momentum (baroclinic gradient $(-\frac{g}{\rho_0} \int_z^{\eta} \nabla \rho d\zeta)$, horizontal viscosity,
130 Coriolis, earth tidal potential, atmospheric pressure, radiation stress)

131 g acceleration of gravity, in $[\text{ms}^{-2}]$

132 C tracer concentration (e.g., salinity, temperature, sediment etc)

133 ν vertical eddy viscosity, in $[\text{m}^2\text{s}^{-1}]$

134 κ vertical eddy diffusivity, for tracers, in $[\text{m}^2\text{s}^{-1}]$

135 F_h horizontal diffusion and mass sources/sinks

136 The differential system (1-4) is closed with turbulence closure of the generic length-scale model of Umlauf and
137 Burchard (2003), and proper initial and boundary conditions (B.C.) for each differential equation.

138 The 3D domain is first discretized into triangular elements in the horizontal and a series of vertical layers (using
139 hybrid SZ coordinates). The unknown variables are then staggered on triangular prisms as shown in Fig. 2, which
140 resembles a CD grid (Arakawa and Lamb 1977) as well as the $\text{P}^1\text{-P}^{\text{NC}}$ element configuration (Le Roux et al. 2005).

141 In the first step, SELFE solves the coupled equations (1) and (3) together with their boundary conditions, with a
142 semi-implicit Galerkin Finite Element method (FEM). The linear pair of $\text{P}^1\text{-P}^{\text{NC}}$ element configuration is used to
143 approximate the elevation and horizontal velocity respectively. The implicit terms include elevation gradient,
144 vertical viscosity, the bottom B.C. for Eq. (1), and the divergence term in Eq. (3), all of which impose severe
145 stability constraints. The time stepping is done using a 2nd-order Crank-Nicolson method, i.e., with the implicitness
146 factor being 0.5 (in practice a value slightly larger than 0.5 is used for robustness). The unknown velocities (defined
147 at side centers) are first eliminated from the equations with the aid from the bottom boundary layer, resulting in an
148 integral equation for the unknown elevations alone, which can be efficiently solved with a parallel solver (Jacobian

149 Conjugate Gradient) (ZB08). The momentum equation is then solved with a Galerkin FEM along each vertical
 150 column of a side. After the horizontal velocity and elevation are found, the vertical velocity is then solved from Eq.
 151 (2) with a Finite Volume method (FVM) along each prism. The volume conservation ensured by FVM serves as the
 152 foundation for the mass conservative transport solver, which also employs a FVM (with either 1st-order upwind or
 153 2nd-order explicit TVD method; see Casulli and Zanolli 2005), because the volume conservation guarantees
 154 constancy condition for the transport equation. Note that the volume conservation in SCHISM is only approximate
 155 in the sense that there is a closure error for the vertical velocity due to the different methods used to solve the two
 156 forms of the continuity equation (FEM for Eq. (3) vs FVM for Eq. (2)). Solution of the 2.5 turbulence closure
 157 equations and update of the vertical grid (including the marking of wetting and drying nodes/sides/elements)
 158 constitute the remaining operations in a time stepping loop. More details can be found in ZB08.

159 The CD grid used in SELFE is instrumental in its ability to easily maintain geostrophic balance, as both velocity
 160 components (u, v) are explicitly modelled. This is a key difference from UnTRIM-family of models (Casulli and
 161 Cattani 1994) which uses a C grid, where special treatment has to be made to properly maintain the geostrophic
 162 balance (Zhang et al. 2004; Ham et al. 2007). In addition, due to the finite-difference method used in the UnTRIM-
 163 family of models, only *orthogonal* UG grids can be used, which proves to be restrictive in practice. On the other
 164 hand, the FEM framework used in SELFE (and SCHISM) allows generic non-orthogonal UG's to be used. In fact,
 165 the model has a high tolerance for skew (non-orthogonal) elements.

166 A critical feature of SELFE is the use of Eulerian-Lagrangian method (ELM) to treat the momentum advection term:

$$167 \frac{D\mathbf{u}}{Dt} \cong \frac{\mathbf{u}(\mathbf{x}, t^{n+1}) - \mathbf{u}(\mathbf{x}^*, t^n)}{\Delta t} \quad (5)$$

168 where ' n ' and ' $n+1$ ' denote time step levels, Δt is the time step, \mathbf{x} is a shorthand for (x, y, z) , and \mathbf{x}^* is the location of
 169 the foot of characteristic line (FOCL), calculated from the characteristic equation:

$$170 \frac{D\mathbf{x}}{Dt} = \mathbf{u} \quad (6)$$

171 The location \mathbf{x}^* is found via a backtracking step, standard in an ELM, via backward integration of Eq. (6) starting
 172 from a *given* location (\mathbf{x}), which is in our case a side center at whole level where the horizontal velocity \mathbf{u} is defined.
 173 The fixed starting location (Eulerian framework) followed by a Lagrangian tracking step gives the name Eulerian-
 174 Lagrangian method. Therefore the ELM consists of two major steps: a backtracking step (Fig. 3a) and an
 175 interpolation step at FOCL (Fig. 3b). We further sub-divide the tracking step into smaller intervals (based on local
 176 flow gradients), and use a 2nd-order Runge-Kutta method (mid-point method) within each interval, in order to
 177 accurately track the trajectory (cf. the ELM test in Section 3). Although exact integration methods have been
 178 proposed (Ham et al. 2006), their implementation is complicated for a 3D (triangular and quadrangular) prism and in
 179 the exceptional cases of wetting and drying interfaces. The interpolation step serves as an important control for
 180 numerical diffusion/dispersion in the ELM, and we therefore experimented with several options as shown below.
 181 However, before we get to this, we first explain how SELFE converts the velocities at sides to the velocities at
 182 nodes, as the latter are required in the interpolation of the velocities along the characteristic line and at FOCL (Fig.
 183 3ab).

184 As explained by Danilov (2012), the conversion method used bears important ramifications: judicious averaging
 185 (e.g., from side to elements or to node etc.) may greatly reduce the need later on for filters to remove the inertial
 186 spurious modes while still keeping the inherent numerical dissipation low. In fact, one could have used the
 187 discontinuous velocity calculated within each element to carry out the backtracking, but this would introduce
 188 insufficient amount of dissipation to suppress the inertial modes.

189 In the first approach ('MA' hereafter), we use inverse distance weights to interpolate from velocities at surrounding
 190 sides onto a node (Fig. 4a). This introduces diffusion which may be excessive in our experience, and therefore no
 191 further stabilization (via filters or viscosity) is required for this approach (see the discussion of stabilization in
 192 Danilov 2012). This approach works well in shallow waters especially for the inundation process, as numerical
 193 stability often trumps the order of accuracy there. The 2nd approach ('MB' hereafter) is more elegant and utilizes the
 194 (linear) shape function in FEM within each element to calculate the node velocities. This is equivalent to using the
 195 P^{NC} non-conformal shape function (Le Roux et al. 2005) as one essentially interpolates based on information at sides
 196 (Fig. 4b). Because each element produces a velocity vector at each of its 3 nodes, the final node velocity is the

197 simple average of the values calculated from all of the surrounding elements (Fig. 4b). As we will demonstrate with
 198 a simple test in the next section, this approach introduces much less dissipation, but does exhibit inertial spurious
 199 modes. As a result, further stabilization is required. To this end, SELFE uses a 5-point Shapiro filter (Shapiro 1970)
 200 as illustrated in Fig. 5a; the velocity at a side ‘0’ is filtered as:

$$201 \quad \tilde{\mathbf{u}}_0 = \mathbf{u}_0 + \frac{\gamma}{4}(\mathbf{u}_1 + \mathbf{u}_2 + \mathbf{u}_3 + \mathbf{u}_4 - 4\mathbf{u}_0), \quad (7)$$

202 with the strength usually set as $\gamma=0.5$. We will show that the filter is analogous to a viscosity implementation in the
 203 next section. It proves to be very effective in removing the sub-grid scale inertial spurious modes; however, it
 204 introduces too much dissipation in the eddying regime, and we’ll present a better alternative in SCHISM in the next
 205 section.

206 Once the node velocities are found via MA or MB, the interpolation at the FOCL is carried out in 3D space. A
 207 simple linear interpolation is used in the vertical dimension as the results from the cubic-spline interpolation turned
 208 out to be similar, due to more confined spatial scales and smaller grid sizes in the vertical. The horizontal
 209 interpolation can be done using either a simple linear shape function based on all of the nodes of the containing
 210 element (‘LI’ hereafter; Fig. 3b), or a higher-order dual kriging method (‘KR’ hereafter) suggested by Le Roux et al.
 211 (1997). The latter requires larger stencil around the FOCL, and for best parallel efficiency we use a 2-tier
 212 neighborhood as shown in Fig. 3b. Given a total of N nodes available in the 2-tier neighborhood, the interpolation
 213 function is constructed as (Le Roux 1997):

$$214 \quad f^h(x, y) = (\alpha_1 + \alpha_2 x + \alpha_3 y) + \sum_{i=1}^N \beta_i K(r_i) \quad (8)$$

215 where the first 3 RHS terms inside the parentheses represent a mean drift (modeled as a linear function), and the 2nd
 216 terms is the fluctuation part, α_j, β_i are unknown coefficients, and r_i is the distance between (x, y) and (x_i, y_i) , with i
 217 being a node. The following forms of the generalized covariance function are commonly used (Le Roux et al. 1997):

$$218 \quad K(r) = -r, \quad r^2 \log(r), \quad r^3, \quad -r^5, \quad r^7 \quad (9)$$

219 with increasing dispersion for the higher-degree functions; therefore in practice, the last two functions are seldom
 220 used. In the following we will refer to the first 3 functions as ‘KR1’, ‘KR2’ and ‘KR3’ respectively.

221 The equations to solve for the unknown coefficients are:

$$222 \quad \left\{ \begin{array}{l} f^h(x_i, y_i) = d_i, \quad 1 \leq i \leq N \\ \sum_{i=1}^N \beta_i = 0 \\ \sum_{i=1}^N x_i \beta_i = 0 \\ \sum_{i=1}^N y_i \beta_i = 0 \end{array} \right. \quad (10)$$

223 where d_i are given data at each node. The 1st equation in (10) indicates that the dual kriging is an exact interpolator,
 224 and the other 3 equations are derived from minimization of the variance of estimation error (Le Roux et al. 1997).
 225 Note that the matrix of Eq. (10) is dependent only on geometry and therefore can be inverted and stored before the
 226 time stepping loop to achieve greater efficiency. After the coefficients are found, the interpolation at FOCL is done
 227 via Eq. (8).

228 The smaller stencil used here compared to that used by Le Roux et al. (1997) leads to larger numerical dispersion.
 229 Therefore an effective method must be found to control the dispersion, and we will show how this is done in
 230 SCHISM in the next section.

231 We conclude this section by noting that the various schemes presented above can be freely combined, resulting in
 232 schemes like ‘MA-LI’, ‘MB-KR2’ etc.

233

234 **3. Revisions in SCHISM**

235 In this section we present new advection schemes for the transport and momentum equations used by SCHISM. Our
 236 focus is on the eddying regime but the reduced dissipation enabled by the new schemes proves largely beneficial for
 237 the shallow environment as well and we have successfully tested these schemes in the non-eddying regime (Ye et al.
 238 submitted).

239 **3.1 Tracer advection scheme: TVD²**

240 The 2nd-order TVD scheme in SELFE is explicit in 3D space and thus subject to the Courant condition, which
 241 comprises of horizontal and vertical fluxes across each of the prism faces (Casulli and Zanolli 2005). The restriction
 242 related to the vertical fluxes is especially severe due to smaller grid size used in the vertical dimension, and therefore
 243 a large number of sub-cycles within each time step are usually required. To partially mitigate the issue, a hybrid
 244 upwind-TVD approach can be used in which the more efficient upwind scheme, with an implicit treatment of the
 245 vertical fluxes, is used when the flow depth falls below a given threshold (with the assumption that stratification is
 246 usually much smaller in the shallows). However, this approach does not work in deeper depths of eddying regime, as
 247 large vertical velocities are not uncommon along steep bathymetric slopes. Together with the fact that a large
 248 number of vertical levels are usually required in the eddying regime, the explicit scheme leads to subpar
 249 computational performance and usually takes over 90% of the total CPU time.

250 We therefore develop an implicit TVD scheme in the vertical dimension in SCHISM. We start from the FVM
 251 formulation of the 3D transport equation (4) at a prism i :

$$252 \quad C_i^{n+1} = C_i^n - \frac{\Delta t}{V_i} \sum_{j \in S^-} |Q_j| (C_i - C_j) - \frac{\Delta t}{V_i} \sum_{j \in S} Q_j C_{jr} + \frac{A_i \Delta t}{V_i} \left[\left(\kappa \frac{\partial C}{\partial z} \right)_{i,k} - \left(\kappa \frac{\partial C}{\partial z} \right)_{i,k-1} \right] + \frac{\Delta t}{V_i} \int_{V_i} F_h dV$$

253 (11)

254 where C_j is the concentration at the neighboring prism of i across a prism face $j \in S = S^+ \cup S^-$, with S^+/S^- denoting
 255 outflow/inflow faces (which can be horizontal or vertical) respectively, V_i is the prism volume, A_i is the area of the
 256 associated surficial triangular element, and Q_j is the flux at a face. In Eq. (11) we have utilized the volume
 257 conservation in a prism (which is enforced by the solution of the vertical velocity): $\sum_{j \in S^-} |Q_j| = \sum_{j \in S^+} |Q_j|$. We
 258 have also approximated the concentration at a face as the sum of an upwind and a correction part as:

$$259 \quad C|_j = C_{jup} + C_{jr}. \quad (12)$$

260 Note that in the 2nd term of RHS of Eq. (11), we have $C_j = C_{jup}$ as j is an inflow face. In addition, we have
 261 intentionally left out the time level in some terms in (11) as they will be treated explicitly or implicitly in the
 262 following.

263 We split the solution of Eq. (11) into 3 sub-steps:

$$264 \quad C_i^{m+1} = C_i^m + \frac{\Delta t_m}{V_i} \sum_{j \in S_H^-} |Q_j| (C_j^m - C_i^m) - \frac{\Delta t_m}{V_i} \sum_{j \in S_H} Q_j \hat{\psi}_j^m, \quad (m = 1, \dots, M) \quad (13)$$

$$265 \quad \tilde{C}_i = C_i^{M+1} + \frac{\Delta t}{V_i} \sum_{j \in S_V^-} |Q_j| (\tilde{C}_j - \tilde{C}_i) - \frac{\Delta t}{V_i} \sum_{j \in S_V} Q_j (\Phi_j + \Psi_j), \quad (j = k_b, \dots, N_z) \quad (14)$$

$$266 \quad C_i^{n+1} = \tilde{C}_i + \frac{A_i \Delta t}{V_i} \left[\left(\kappa \frac{\partial C}{\partial z} \right)_{i,k}^{n+1} - \left(\kappa \frac{\partial C}{\partial z} \right)_{i,k-1}^{n+1} \right] + \frac{\Delta t}{V_i} \int_{V_i} F_h^n dV, \quad (k = k_b, \dots, N_z) \quad (15)$$

267 The 1st step Eq. (13) solves the horizontal advection part (for all 3D prisms i), the 2nd step Eq. (14) deals with the
 268 vertical advection part (where k_b is the bottom level index and N_z is the surface level index), and the last step Eq.
 269 (15) tackles the remaining terms. We could have combined the 1st and 3rd steps into a single step at the expense of
 270 efficiency, because sub-cycling is used in the 1st step. In Eq. (13), sub-cycling in M sub-steps is required because of

271 the horizontal Courant number condition, Δt_m is the sub-time step used, and $\hat{\psi}_j^m$ is a standard TVD limiter function.
 272 Eq. (13) is then solved with a standard TVD method. The last step (15) requires the solution of a simple tri-diagonal
 273 matrix. So we will only focus on the 2nd step.

274 Following Duraisamy and Baeder (2007, hereafter DB07), we use two limiter functions in Eq. (14): Φ_j is the space
 275 limiter and Ψ_j is the time limiter – thus the name TVD². The origin of these two limiters is the approximation Eq.
 276 (12) via a Taylor expansion in both space *and* time (DB07):

$$277 \quad C_j^{n+1/2} = C_{jup}^{n+1} + \Phi_j + \Psi_j = C_{jup}^{n+1} + \mathbf{r} \bullet [\nabla C]_{jup}^{n+1} - \frac{\Delta t}{2} \left[\frac{\partial C}{\partial t} \right]_{jup}^{n+1} \quad (16)$$

278 Note that the interface value is taken at time level $n+1/2$ to gain 2nd-order accuracy in time. The vector \mathbf{r} points from
 279 prism center jup to face center j . Due to the operator splitting method, C^{n+1} now actually corresponds to \tilde{C} .
 280 Customary in a TVD method, we then replace the last 2 terms with limiter functions:

$$281 \quad C_j^{n+1/2} = \tilde{C}_{jup} + \frac{\phi_j}{2} (\tilde{C}_{jD} - \tilde{C}_{jup}) - \frac{\psi_j}{2} (\tilde{C}_{jup} - C_{jup}^{M+1}) \quad (17)$$

282 and so:

$$283 \quad \Phi_j = \frac{\phi_j}{2} (\tilde{C}_{jD} - \tilde{C}_{jup}), \Psi_j = -\frac{\psi_j}{2} (\tilde{C}_{jup} - C_{jup}^{M+1}) \quad (18)$$

284 where ‘ jD ’ stands for the downwind prism of i along the face j , and ϕ_j and ψ_j are 2 limiter functions in space and
 285 time respectively. Note that $\phi_j = \psi_j = 1$ leads to 2nd-order accuracy in both space and time.

286 Substituting Eq. (18) into (14) and after some algebra we obtain a nonlinear equation for the unknown
 287 concentration:

$$288 \quad \tilde{C}_i + \frac{\frac{\Delta t}{V_i} \sum_{j \in S_V^-} |\mathcal{Q}_j| \left[1 + \frac{1}{2} \left(\sum_{p \in S_V^+} \frac{\phi_p}{r_p} - \phi_j \right) \right] (\tilde{C}_i - \tilde{C}_j)}{1 + \frac{\Delta t}{2V_i} \sum_{j \in S_V^+} |\mathcal{Q}_j| \left(\sum_{q \in S_V^-} \frac{\psi_q}{s_q} - \psi_j \right)} = C_i^{M+1} \quad (19)$$

289 where r_p and s_q are upwind and downwind ratios respectively:

$$290 \quad r_p = \frac{\sum_{q \in S_V^-} |\mathcal{Q}_q| (\tilde{C}_q - \tilde{C}_i)}{|\mathcal{Q}_p| (\tilde{C}_i - \tilde{C}_p)}, p \in S_V^+ \quad (20)$$

$$s_q = \frac{(\tilde{C}_i - C_i^{M+1}) \sum_{p \in S_V^+} |\mathcal{Q}_p|}{|\mathcal{Q}_q| (\tilde{C}_q - C_q^{M+1})}, q \in S_V^-$$

291 DB07 showed that a sufficient TVD condition for Eq. (19) is that the coefficient of the 2nd LHS term be non-
 292 negative, i.e.:

$$293 \quad 1 + \frac{1}{2} \left(\sum_{p \in S_V^+} \frac{\phi_p}{r_p} - \phi_j \right) \geq 0 \quad (21)$$

294
$$1 + \frac{\Delta t}{2V_i} \sum_{j \in S_V^+} |Q_j| \left(\sum_{q \in S_V^-} \frac{\psi_q}{s_q} - \psi_j \right) \geq \delta > 0 \quad (22)$$

295 where δ is a small positive number. Eq. (21) can be satisfied with any choice of standard limiter functions in space,
 296 and Eq. (22) must be solved together with Eq. (19) iteratively, because ψ and s_q are functions of \tilde{C} . We need to
 297 discuss 3 scenarios for prism i :

298 (1) vertically convergent flow: in this case, the outer sum in Eq. (22) is 0, so the inequality is always true;

299 (2) divergent flow: the numerator of the 2nd LHS term in Eq. (19) is 0, and so $\tilde{C}_i = C_i^{M+1}$;

300 (3) uni-directional flow (either upward or downward): in this case, prism i has exactly 1 inflow and 1 outflow face
 301 vertically, so a sufficient condition for Eq. (22) is:

302
$$1 - \frac{\Delta t}{2V_i} |Q_j| \psi_j \geq \delta > 0, j \in S_V^+ \quad (23)$$

303 Therefore we choose the following form for the limiter:

304
$$\psi_j = \max \left[0, \min \left[1, \frac{2(1-\delta)V_i}{|Q_j| \Delta t} \right] \right], j \in S_V^+ \quad (24)$$

305 where we have imposed a maximum of 1 in an attempt to obtain 2nd-order accuracy in time. Note that the limiter is a
 306 function of the vertical Courant number: it decreases as the Courant number increases. Eqs. (19) and (24) are then
 307 solved using a simple Picard iteration method starting from $\psi=0$ everywhere, and fast convergence within a few
 308 iterations is usually observed.

309 Simple benchmark tests indicate that TVD² is accurate for a wide range of Courant numbers as found in typical
 310 geophysical flows (Ye et al. submitted). The accuracy and efficiency of TVD² will also be shown in Section 5. It
 311 works equally well in eddying and non-eddying regimes, from very shallow to very deep depths, and is thus ideal for
 312 cross-scale applications.

313

314 **3.2 Viscosity**

315 Danilov (2012) demonstrated the importance of the momentum advection and stabilization schemes in the eddying
 316 regime for UG models. Beside accuracy consideration, prevention of spurious modes is an important goal, which
 317 can be done via viscosity, filtering, and/or averaging of velocity fields (e.g., from element to node etc). As the
 318 Shapiro filter, which is designed to remove the spurious modes in SELFE, is too dissipative in the eddying regime,
 319 we replace it with an effective horizontal viscosity scheme in SCHISM.

320 Most geophysical fluid dynamic models use horizontal viscosity to add dissipation to the numerical scheme in order
 321 to control sub-grid scale instabilities, e.g. due to cascading of enstrophy toward the smallest resolved scales (Griffes
 322 and Hallberg 2000). In other words, one of the main goals of the viscosity is to remove the unresolved sub-grid
 323 scales but preserve the resolved scales as much as possible. The new viscosity scheme presented here is therefore
 324 designed more to filter out spurious modes than to represent the actual physical horizontal mixing process.

325 We start with a demonstration that the traditional Laplacian viscosity loses its effectiveness on generic UGs. While
 326 there are different ways to implement the Laplacian viscosity on UGs, we present a particular way catered to the
 327 specificity of SCHISM; nevertheless the conclusion here applies to other implementations as well. Consider the
 328 stencil depicted in Fig. 5a; the horizontal viscosity term at the side center ‘0’ is given by:

329
$$\nabla \cdot (\mu \nabla u) \Big|_0 \cong \frac{\mu_0}{A_I + A_{II}} \oint_{\Gamma} \frac{\partial u}{\partial n} d\Gamma \quad (25)$$

330 where Γ is the boundary PQRS (Fig. 5a), and we assume the viscosity μ_0 to be constant in the stencil. The formula
 331 for the viscosity term for the v -velocity is similar. The derivatives are evaluated using the linear shape functions

332 defined inside the 2 smaller triangles formed by joining the 3 side centers (012 and 034 in Fig. 5a), and are constant
 333 within each triangle:

$$334 \quad \left. \frac{\partial u}{\partial x} \right|_I = \frac{1}{A_I} [u_1(y_Q - y_P) + u_2(y_R - y_Q) + u_0(y_P - y_R)] \quad (26)$$

$$\left. \frac{\partial u}{\partial y} \right|_I = -\frac{1}{A_I} [u_1(x_Q - x_P) + u_2(x_R - x_Q) + u_0(x_P - x_R)]$$

335 with a similar form for element *II*. The final form for the viscosity is then:

$$336 \quad \nabla \cdot (\mu \nabla u)|_0 = \frac{\mu_0}{A_I + A_{II}} \left\{ \begin{array}{l} \frac{1}{A_I} [u_1 \overrightarrow{PQ} \cdot \overrightarrow{PR} + u_2 \overrightarrow{RQ} \cdot \overrightarrow{RP} - u_0 |\overrightarrow{PR}|^2] + \\ \frac{1}{A_{II}} [u_3 \overrightarrow{RP} \cdot \overrightarrow{RS} + u_4 \overrightarrow{PR} \cdot \overrightarrow{PS} - u_0 |\overrightarrow{PR}|^2] \end{array} \right\} \quad (27)$$

337 where proper linear vertical interpolation has been made to bring u_m ($m=1, \dots, 4$) onto the same horizontal plane as u_0 .
 338 For uniform grid with equilateral triangles, Eq. (27) becomes:

$$339 \quad \nabla \cdot (\mu \nabla u)|_0 = \frac{\mu_0}{\sqrt{3}A_I} (u_1 + u_2 + u_3 + u_4 - 4u_0) \quad (28)$$

340 which is equivalent to the 5-point Shapiro filter (cf. Eq. (7)), with filter strength $\gamma = \frac{4\mu_0 \Delta t}{\sqrt{3}A_I} \equiv \frac{4D}{\sqrt{3}}$ (with D being a
 341 diffusion number). However, for obtuse triangles, some coefficients of u_m ($m=1, 2, 3, 4$) in Eq. (27) become negative,
 342 and the viscosity then behaves like an amplifier (Shapiro 1970), and thus loses its utility of smoothing. This calls for
 343 a filter-like viscosity implementation as in Eq. (28) for UGs, and we use this equation to replace the Shapiro filter
 344 for generic UG's. Danilov and Androsov (2015) used a similar form for viscosity. For boundary sides the viscosity
 345 term is omitted as B.C. is applied there instead.

346 The bi-harmonic viscosity is often superior to the Laplacian viscosity as it is more discriminating in removing sub-
 347 grid instabilities without adversely affecting the resolved scales of flow (Griffies and Hallberg 2000). The bi-
 348 harmonic viscosity can be implemented by applying the Laplacian operator twice. Referring to Fig. 5c, we have:

$$349 \quad -\lambda \nabla^4 u|_0 = -\lambda \gamma_3 (\nabla^2 u_1 + \nabla^2 u_2 + \nabla^2 u_3 + \nabla^2 u_4 - 4\nabla^2 u_0) =$$

$$\frac{\gamma_2}{\Delta t} [7(u_1 + u_2 + u_3 + u_4) - u_{1a} - u_{1b} - u_{2a} - u_{2b} - u_{3a} - u_{3b} - u_{4a} - u_{4b} - 20u_0] \quad (29)$$

350 where λ is a hyper viscosity in m^4/s , $\gamma_3 = 1/(\sqrt{3}A_I)$ and $\gamma_2 = \lambda \gamma_3^2 \Delta t$ is a diffusion-number-like dimensionless
 351 constant. We found that in practice $\gamma_2 \leq 0.025$ is sufficient to suppress inertial spurious modes, and so in this paper
 352 we set $\gamma_2=0.025$ for all test cases.

353

354 **3.3 Momentum advection scheme**

355 As we discussed in Section 2, the interpolation method used at FOCL has important ramifications. Since the dual
 356 kriging interpolators generate numerical dispersion (over-/under-shoots or excess mass field), we need an effective
 357 method to control the excess mass field; otherwise the dispersion would severely aggravate the inertial spurious
 358 modes. We use the ELAD method of Shchepetkin and McWilliams (1998) for this purpose. The essence of ELAD is
 359 to iteratively diffuse the *excess field*, instead of the original signal, using a diffusion operator/smoothing. The
 360 viscosity scheme presented in the previous sub-section is used as the diffusion operator. The procedure is
 361 summarized as follows:

362 1) Find the local max/min at FOCL. Assuming that the prism at FOCL starting from a side j and level k is
 363 (kf, nf) , where nf is the element index and kf is the vertical index, the max/min are found in the prism (kf, nf)
 364 as:

$$365 \quad \begin{aligned} u_{k,j}^{\max} &= \max_{l=1:3, k=-1, 0} u_{kf+k, im(l, nf)} \\ u_{k,j}^{\min} &= \min_{l=1:3, k=-1, 0} u_{kf+k, im(l, nf)} \end{aligned} \quad (30)$$

366 where $im()$ enumerates 3 nodes of an element.

367 2) The excess field associated with (k, j) is:

$$368 \quad \varepsilon_{k,j}^{(1)} = \max \left[0, u_{k,j}^{n+1,1} - u_{k,j}^{\max} \right] + \min \left[0, u_{k,j}^{n+1,1} - u_{k,j}^{\min} \right] \quad (31)$$

369 where $u_{k,j}^{n+1,1}$ is the interpolated value at FOCL.

370 3) Apply a global diffusion operator to ε to obtain estimated velocity at the next iteration:

$$371 \quad u_{k,j}^{n+1,2} = u_{k,j}^{n+1,1} + \mu' \Delta t \nabla^2 \varepsilon_{k,j}^{(1)}, \quad \forall j, k \quad (32)$$

372 and we use the 5-point filter with maximum strength (cf. (Eqs. (7,28)):

$$373 \quad u_{k,j}^{n+1,2} = u_{k,j}^{n+1,1} + \frac{1}{8} \left[\varepsilon_{k,1}^{(1)} + \varepsilon_{k,2}^{(1)} + \varepsilon_{k,3}^{(1)} + \varepsilon_{k,4}^{(1)} - 4\varepsilon_{k,j}^{(1)} \right] \quad (33)$$

374 where subscripts 1-4 are the 4 adjacent sides of j (Fig. 5a);

375 4) Calculate the new excess field using $u_{k,j}^{n+1,2}$ in 2) and apply the filter 3) again to find the velocity at the next
 376 iteration $u_{k,j}^{n+1,3}$. Iterate until the excess field falls below a prescribed threshold. In practice, 10 iterations
 377 are usually sufficient to bring the excess field below an acceptable level (10^{-4} m/s); the remaining excess
 378 field is then further smoothed with the viscosity.

379 The filter in Eq. (33) is conservative in the sense that it only redistributes excess mass and does not introduce any
 380 additional mass. This is similar in spirit to the conservative scheme of Gravel and Staniforth (1994) but appears
 381 simpler in implementation. At a boundary side j , Eq. (33) is modified in order to maintain the conservation:

$$382 \quad u_{k,j}^{n+1,2} = u_{k,j}^{n+1,1} + \frac{1}{8} \left[\varepsilon_{k,1}^{(1)} + \varepsilon_{k,2}^{(1)} - 2\varepsilon_{k,j}^{(1)} \right] \quad (34)$$

383 where subscripts '1' and '2' are the 2 adjacent sides of j (Fig. 5d). Note that since the linear interpolation scheme
 384 (LI) does not introduce local extrema, ELAD is not applied there.

385

386 **3.3.1 A convergence test**

387 A combination of filter and higher-order advection schemes is often used in ocean models. Due to the use of filter,
 388 the actual order of convergence may be lower than what the original scheme is intended, and should be numerically
 389 derived using benchmark tests. As ELM is not a conventional method and direct comparison with upwind-type
 390 methods is often lacking in the literature, we demonstrate the order of convergence of various ELM schemes
 391 employed in SCHISM using a rotating Gauss hill test. In this test, we fix the advective velocity field as:

$$392 \quad \begin{cases} u = -\omega y \\ v = \omega x \\ w = 0 \end{cases} \quad (35)$$

393 with the period of rotation $T_0=3000s$, and angular frequency $\omega=2\pi/T_0$. We then use the temperature as a proxy for
 394 the velocity; in other words, we define the temperature at side centers and whole levels (just like velocity), convert
 395 the side temperature to node temperature, interpolate its value at FOCL, and apply ELAD (for dual kriging ELM) in
 396 exactly the same way as we did for velocity. Since we are only concerned with pure advection problem, no viscosity
 397 is applied to the ‘temperature’. This way we can study the momentum advection schemes in isolation from other
 398 parts of the model. Initially the Gauss hill of unit amplitude is defined as:

$$399 \quad T = \exp \left[-\frac{(x-x_0)^2 + (y-y_0)^2}{\sigma^2} \right] \quad (36)$$

400 where $x_0=0$, $y_0=1800m$, and $\sigma=850m$. We generate a circular grid of radius of 3600m with essentially uniform
 401 triangles using DistMesh (Persson and Strang 2004). The side length of triangles is varied in the convergence study
 402 as 400m, 200m, 100m, and 50m. The time step used is 300s for $\Delta x=400m$ and adjusted for other cases such that the
 403 Courant number remains constant, and the 2nd-order Runge-Kutta method is used to calculate the characteristic line.
 404 For kriging interpolators (‘KR’), ELAD is applied with a threshold of 10^{-4} and maximum of 10 iterations (we have
 405 also tried a maximum of 100 iterations and the results are similar).

406 The results with $\Delta x=50m$ after 1 rotation from various advection schemes are compared with each other and the
 407 exact solution in Fig. 6. The two MA schemes have almost no under-/over-shoots (MA-KR3 has a very small
 408 undershoot on the order of -10^{-20}), whereas all MB schemes have some dispersion. MB-LI and MB-KR1 have no
 409 overshoots, but have undershoots of $-2.e-4$ and $-1.e-4$ respectively. On the other hand, MB-KR2 and MB-KR3 lead
 410 to much larger overshoots (~ 0.027 ; note the distortion near the center of the hill) and smaller undershoots of $-4.e-5$
 411 and $-6.e-5$ respectively. These results are an indication of larger numerical diffusion/dissipation inherent in all MA
 412 schemes. Note that ELAD is not applied to MB-LI or MA-LI.

413 The convergence curves from various schemes are summarized in Fig. 7. Highest convergence rate (~ 1.93) is
 414 achieved with MB-KR2 and MB-KR3. However, this is mostly due to the larger errors at coarser resolutions. In
 415 terms of RMSE, the best accuracy is achieved with MB-LI followed closely by MB-KR1. The discrepancy between
 416 the convergence rate and absolute error as shown here is probably not uncommon in ocean models and has
 417 important implications. The leading-order truncation error consists of two parts: a coefficient and an exponential
 418 term, and both are equally important. Since the order of convergence is only related to the 2nd part, a ‘lower-order’
 419 scheme such as MB-LI can still achieve better accuracy if it has a smaller ‘coefficient’. While some higher-order
 420 methods may theoretically lead to better convergence rate, their accuracy may require an unrealistically fine
 421 resolution. Another important consideration is that the use of ‘smoothers’ in the higher-order methods may also
 422 degrade the convergence rate. Despite their relatively lower convergence rates (~ 1.5), the smaller RMSE and
 423 superior shape-preserving ability achieved by MB-LI and MB-KR1 as demonstrated in Figs. 6 & 7 make them better
 424 choices for practical applications with SCHISM. Although the test is done with a simple case here and the values of
 425 RMSEs might not directly translate to realistic cases, our experience suggests that the *relative* performance of each
 426 scheme revealed from this simple test is also representative in realistic cases. We therefore use MB-LI for the rest of
 427 the paper. However, we should remark that the superior stability of MA schemes makes them ideal for shallow-
 428 water environment, and the better accuracy achieved by MA-KR3 may partially mitigate the induced numerical
 429 dissipation. Therefore a judicious combination of MA and MB schemes may be ideal for some applications, and this
 430 will be explored in future research.

431

432 **4. Extension to mixed grids**

433 Quads are computationally more economical and in the case of a FEM model like SCHISM, the bilinear shape
 434 function associated with quad elements also gives better accuracy than that for triangular elements. Since the ratio
 435 between the velocity and elevation spaces becomes smaller with the quad grid, the inertial spurious modes can also
 436 be reduced (Danilov and Androsov 2015).

437 Most schemes in SCHISM are agnostic with respect to element type and therefore their extension to quads is
 438 straightforward. The main changes are summarized below. For FEM formulation, bilinear shape function is used for
 439 quads, and the integrals are evaluated either analytically or using a 4-point (cubic) Gauss quadrature. Note that the
 440 idea of LSC² and shaved cell technique can be trivially adapted to quads as well. The changes to TVD² are minimal
 441 due to the FVM used. Therefore in the following we focus on the new viscosity and ELAD schemes.

442 For the reason explained in Section 3.2 (i.e. to prevent negative coefficients), we will derive the viscosity form on
 443 uniform quads. Referring to Fig. 5b, the viscosity term is:

$$444 \quad \nabla \cdot (\mu \nabla u)|_0 = \frac{\mu_0}{A_I + A_{II}} \left[\left(\frac{\partial u}{\partial n} \right)_1 + \left(\frac{\partial u}{\partial n} \right)_2 + \left(\frac{\partial u}{\partial n} \right)_3 + \left(\frac{\partial u}{\partial n} \right)_4 + \left(\frac{\partial u}{\partial n} \right)_5 + \left(\frac{\partial u}{\partial n} \right)_6 \right] \quad (37)$$

445 And the normal derivatives are evaluated inside the 2 smaller squares formed by the dashed lines. For convenience
 446 we rotate the coordinate frame so that the x - and y -axes are perpendicular to lines (0,1) and (1,2) respectively and the
 447 origin is located at the center of element I (note that the viscosity term is invariant under coordinate rotation). The
 448 transformation from (x,y) to local coordinates (ν, ξ) is then simply: $x=b\nu$ and $y=b\xi$, where $b = \sqrt{2}a/4$ and a is the
 449 element side length. The 4 shape functions associated with points 0,1,2,3 are:

$$450 \quad \varphi_i(x, y) = \frac{1}{4} \left(1 + \xi_i \frac{x}{b} \right) \left(1 + \nu_i \frac{y}{b} \right), \quad (i = 1, \dots, 4) \quad (38)$$

451 where $|\xi_i|=|\nu_i|=1$ are the local coordinates of the 4 points. Unlike in the case of triangles, the derivatives of u are no
 452 longer constant within each square but need to be evaluated using the derivatives of the shape functions (38). The
 453 final form is:

$$454 \quad \nabla \cdot (\mu \nabla u)|_0 = \gamma_4 (u_1 + u_3 + u_4 + u_6 - 4u_0) \quad (39)$$

455 where $\gamma_4 = \mu_0/(2a^2)$. Note the absence of points 2 and 5 here. Eq. (39) is analogous to the traditional 5-point Laplacian
 456 operator for structured-grids and also to the 5-point viscosity for the triangles Eq. (28). Therefore the viscosity for a
 457 mixed grid involves only the 4 nearest adjacent sides, regardless of whether the element is triangular or
 458 quadrangular. The bi-harmonic viscosity for mixed triangular-quadrangular elements can be readily derived using
 459 Eq. (39) and the first half of Eq. (29). Since the ELAD operator is built on the Laplacian viscosity, Eqs. (33,34) can
 460 be easily extended to include quad elements as well.

461 The combination of LSC² vertical grid (Zhang et al. 2015) and horizontal mixed-element grids results in an
 462 extremely flexible grid system that has great practical applications. We demonstrate this with a toy problem for
 463 coastal ocean-estuary-river system depicted in Fig. 8. Since the tracer concentrations are defined at the prism
 464 centers, a row of quads and 1 vertical layer resembles a 1D model (Fig. 8c). Similarly, a row of quads with multiple
 465 vertical layers leads to 2DV configuration (Fig. 8c). Some parts of the shoals that are sufficiently shallow are
 466 discretized using 1 vertical layer (Fig. 8b), which is a 2DH configuration. The deeper part of the domain is
 467 discretized using full 3D prisms, but with a larger number of layers in the deeper depths than in the shallow depths,
 468 in a typical LSC² fashion (Fig. 8a; Zhang et al. 2015). Different types of grids are *seamlessly* welded into a *single*
 469 SCHISM grid, resulting in greatest efficiency. With some care taken of the consistent bottom friction formulations
 470 across 1D, 2D and 3D (we used a constant drag coefficient of 0.0025 here), the model results show no discontinuity
 471 across different types of grids (Fig. 9). The use of 1D or 2D cells in shallow areas also enhances numerical stability,
 472 as they are well suited and more stable for inundation process than 3D cells; e.g., the crowding of multiple 3D layers
 473 in the shallow depths is not conducive to stability.

474

475 5. Numerical experiments

476 The SCHISM model, with the new developments detailed in previous sections, has been successfully applied by Ye
477 et al. (submitted) to the Chesapeake Bay, by Zhang et al. (2016) to North Sea-Baltic Sea system, and by Stanev et al.
478 (in preparation) to the Black Sea-Turkish Straits system. Here we will focus on benchmarking its performance in the
479 eddying regime, which is the last missing link for our cross-scale model. The 1st case is a simple lock exchange
480 experiment that has been previously used for inter-model assessment. The 2nd case deals with baroclinic instability
481 in a zonally re-entrant channel, and the 3rd case is focused on mesoscale eddies and meanders in the Black Sea. We
482 conclude this section with a brief discussion on the strategy for cross-scale applications.

483 5.1 Lock exchange test

484 Ilicak et al. (2012) assessed the spurious diapycnal mixing in 4 structured-grid models through 5 tests, and found
485 that the amount of spurious diapycnal mixing is proportional to the grid Reynolds number and is also influenced by
486 the viscosity.

487 Their 1st is a simple lock exchange experiment, for which theoretical results for the propagation speed of the gravity
488 current are available (Benjamin 1968). They presented model results from various horizontal and vertical resolutions
489 and used an isopycnal-coordinate model (GOLD) as benchmark. In addition they suggest that the reference potential
490 energy can be used as an effective tool to detect spurious diapycnal mixing.

491 Here we use as close a model set-up to their 1st test as possible in order to help assess the relative performance of
492 SCHISM for this test. The domain is 64km long with a constant depth of 20m and initially each of two water masses
493 of 5°C and 35°C occupies half of the domain. A linear equation of state is used where the water density is linearly
494 dependent on the temperature alone. A main difference in our model set-up is that a larger time step (200s) is used in
495 SCHISM, as it is an implicit model.

496 We conduct convergence study with respect to horizontal and vertical grid resolution as in Ilicak et al. (2012). For
497 simplicity uniform horizontal grids and uniform σ layers are used. Fig. 10(a-d) shows the temperature snapshots
498 from refining the vertical grid. In comparison to Figs. 1 and 2 of Ilicak et al. (2012), we remark that SCHISM results
499 show less noise (using GOLD results as benchmark) especially at higher resolution. The high-resolution SCHISM
500 results also show a thinner pycnocline compared to some of the other models, suggesting acceptable amount of
501 numerical dissipation and dispersion. We have also used two smaller time steps ($\Delta t=150s, 100s$) to further test the
502 model sensitivity, and Fig. 10(e&f) reveals only some subtle differences, mostly in the form of a smaller
503 propagation speed of the fronts than that from $\Delta t=200s$ (Fig. 10d). Decreasing the time step further would eventually
504 degrade the model skill as the CFL number becomes too small (Zhang et al. 2015).

505 The predicted front locations from different horizontal and vertical resolutions are illustrated in Fig. 11ab. With the
506 exception of the coarsest vertical resolution (2 layers), SCHISM results compare favorably with other models,
507 especially at the highest resolution (with the error within 1% of the theoretical value) (Fig. 11a). With the exception
508 of the coarsest horizontal resolution (4km), the model results show only small sensitivity to the horizontal resolution
509 (Fig. 11b). The model's accuracy, convergence and low inherent dissipation are well demonstrated for this
510 baroclinic test.

511 5.2 Reentrant channel

512 Danilov (2012) and Danilov and Wang (private communication) used this case to demonstrate the 'geometric' issues
513 associated with various types of grid-variable arrangements. The domain is essentially a zonal band occupying
514 between 30°N and 45°N. Since periodic boundary condition, which is required if we were to use their smaller
515 domain (20° to 40° long in the zonal direction), is not available in SCHISM, here we use the entire zonal band (from
516 180°W to 180°E), which results in a much larger grid. Note that a quasi-periodic solution is expected for the larger
517 domain (cf. Fig. 13).

518 Initially the salinity is constant at 35PSU (and remains so throughout the simulation), and there is a linear gradient
519 of temperature along the meridional and vertical directions. In addition, a small amount of 'noise' is added to the
520 initial temperature along the zonal direction in order to speed up the development of baroclinic instability (Danilov
521 2012). Therefore the initial temperature is given as:

$$522 \quad T(t = 0) = 25 + \alpha_1 z + \alpha_2 (\varphi - \varphi_0) + \alpha_3 \cos(2\pi\lambda / L_0) \quad (40)$$

523 where $\alpha_1=8.2\times 10^{-3}$ °C/m, $\alpha_2=-0.5566$ °C/(degree latitude), $\alpha_3=0.01$ °C, $L_0=20^\circ$, φ is the latitude, $\varphi_0=30^\circ\text{N}$, and λ
524 is the longitude. The flow is forced by relaxing temperature to its initial distributions in two 1.5° -wide southern and
525 northern relaxation zones near the boundary, with the relaxation scale linearly decreasing from 3 days to zero within
526 these zones. The bottom drag coefficient is kept constant at 0.0025.

527 In the SCHISM set-up, we use the spherical coordinate option implemented with local coordinate frame
528 transformations (Comblen et al. 2009) and the same resolution as in Danilov (2012): $1/7^\circ$ along zonal and $1/6^\circ$ along
529 meridional directions. In the vertical dimension we use 24 S levels to cover the (constant) 1600m depth, with
530 spacing constants of $h_c=30\text{m}$, $\theta_b=0$, $\theta_f=5$ in order to better resolve the surface layers. We use a time step of 300s, and
531 a bi-harmonic viscosity (see Section 3). No explicit horizontal diffusivity is used and the vertical viscosity and
532 diffusivity are calculated from the generic length-scale model with a $k-kl$ configuration (implemented from the
533 formulation of Umlauf and Burchard (2003)). The horizontal grid has 229K nodes, and the simulation runs ~ 200
534 times faster than real time on 216 Intel Xeon cores.

535 Eddies and filaments develop quickly within 0.5 years, and the mean kinetic energy (MKE) reaches a quasi-steady
536 level after ~ 1 year (Fig. 12). The maximum MKE from SCHISM ($\sim 0.07 \text{ m}^2/\text{s}^2$) seems to be close to the scheme MC
537 ($\sim 0.07 \text{ m}^2/\text{s}^2$) but smaller than A-grid ($\sim 0.1 \text{ m}^2/\text{s}^2$) of Danilov (2012); the amplitude of oscillation is also smaller.
538 The snapshots of Sea-Surface Height (SSH) shows certain periodicity along the zonal band but the wavelength is
539 shorter than that used in the initial noise (i.e. 20° ; Eq. (40)) (Fig. 13). To facilitate qualitative comparison with
540 Danilov (2012) and Danilov and Wang (private communication), snapshots, in a 30° zonal band, of SSH and
541 temperature and vorticity at 100m depth are presented in Fig. 14. Qualitatively similar looking eddies and filaments
542 structures are evident in this figure, although our temperature is slightly lower (Fig. 14b). Our filaments also seem to
543 be a little shorter than their best results (Danilov 2012), suggesting slightly larger numerical dissipation in our
544 model. The differences between our and their results may also be partly due to the larger domain we have used.

545

546 5.3 Black Sea

547 The Black Sea, our realistic-model laboratory used in this study to validate the outcome of the numerical methods
548 proposed here, is a nearly enclosed basin of estuarine type (Fig. 15). The run-off from its catchment area (about five
549 times the basin area) is large ($10000\text{-}20000\text{m}^3/\text{s}$) relative to the basin volume ($5.4\times 10^5 \text{ km}^3$). The sea is connected
550 with the Mediterranean Sea through the Turkish Straits System (the Bosphorus Strait, the Sea of Marmara and the
551 Dardanelles Strait). Because the straits are very narrow and shallow the Black Sea is almost completely isolated
552 from world's ocean (Özsoy and Ünlüata 1997; Stanev 2005; Stanev and Lu 2013). The large freshwater flux and the
553 small water exchange with the Mediterranean support a distinct vertical layering limiting the vertical exchange and
554 create a unique chemical and biological environment (the Black Sea is the worlds' largest anoxic basin). Thus this
555 sea can be considered as a natural playground to study geophysical hydrodynamics in the presence of pronounced
556 vertical stratification (salinity changes from $\sim 18\text{PSU}$ at sea surface to $\sim 21\text{PSU}$ at 180 m depth).

557 The Black Sea is a deep estuarine basin. The continental slope in the Black Sea is very variable (Fig. 15b). It is mild
558 in the north-western part, very steep in the southern and eastern part and is carved by deep canyons along the
559 southern coast. This natural setting is also very favorable to study the interaction between stratification and
560 topography as well as the role of planetary and topographic beta-effects (Stanev and Staneva 2000). This interplay
561 results in a general circulation that follows the continental slope and is usually structured in two connected gyre
562 systems encompassing the basin (the Rim Current). This jet-current system is associated with a difference of $\sim 0.2 \text{ m}$
563 between sea levels in the coastal and open sea, with seasonal amplitudes of ~ 10 to 20 cm , and inter-annual variations
564 of ~ 5 to 10 cm (Stanev and Peneva 2002).

565 A comprehensive presentation of SCHISM results for the Black Sea-Turkish Strait System (BS-TSS) is beyond the
566 scope of this paper and has been reported elsewhere (Stanev et al., in preparation). Here we will only focus on
567 assessing the model performance in the eddy regime in the Black Sea. The main DEM source we used is from the
568 GEBCO Digital Atlas (IOC, IHO and BODC 2003). To initialize the model, we use a monthly climatology of
569 salinity and temperature for Black Sea. The 0.2° ECMWF product is used for atmospheric forcings: wind,
570 atmospheric pressure, and air temperature. The 36-km CFSR product (<http://rda.ucar.edu/datasets/ds093.1/>, last
571 accessed Sept. 17 2015) is used for heat and precipitation fluxes due to the lack thereof in the ECMWF product.
572 Discharges at 6 rivers around Black Sea (Fig. 15a) are from monthly mean values, and the (constant) long-term

573 mean flows are used for the 2 major rivers in Azov Sea (Kuban and Don). The excess river flow is compensated by
574 an equivalent outflow through the Bosphorus Straits.

575 We generate a mixed triangular-quadrangular grid of 101K nodes and 172 K element (Fig. 15d). An essentially
576 uniform resolution of 3km is used here to exclude the influence of variable grid resolution on mesoscale processes
577 (see Danilov and Wang (2015) for a detailed discussion on the effects of variable grid resolution on eddies). The
578 refinement near the Bosphorus exit is done for the on-going work that includes the Turkish Strait System. Once the
579 model is fully validated on this grid, we plan to create an UG of variable resolution to refine some coastal areas.
580 Even though the bottom slope is very steep at the shelf break, *no* bathymetry smoothing is done to stabilize the
581 model. A measure of ‘hydrostatic consistency’ (Haney 1991) is given by the Hannah-Wright ratio, defined as
582 $|\Delta h/h_{min}|$, where h_{min} is the minimum depth in an element, and Δh is the maximum difference of depths at nodes
583 in the element (Hannah and Wright 1995). An upper limit of 0.1 for this ratio is usually recommended for terrain-
584 following coordinate models, but Fig. 15c indicates that the ratio is generally much larger than this threshold near
585 the shelf break. We use a LSC² grid in the vertical, with maximum of 53 levels (in the deepest part of Black Sea)
586 and average of 35.4 levels. The time step is set at 120s, and a constant 0.5mm bottom roughness is used. The same
587 bi-harmonic viscosity and vertical viscosity/diffusivity schemes as in Section 5.2 are used here. The model runs 130
588 times faster than real time on 144 CPUs. In contrast, the real-time ratio is reduced to 50 with the explicit TVD
589 method.

590 Fig. 16a shows a typical progression of eddies and meanders inside Black Sea. The Rim Current is accompanied by
591 a series of eddies on both sides, with the anticyclonic mesoscale eddies located between the continental slope and
592 the coast. Their typical radius is between 50 and 100 km as determined by internal radius of deformation. Growing
593 in size some of them detach and propagate into the open sea, e.g., the eddy that is displaced from the south-eastern
594 coastal area and stagnated along the Caucasian coast. Sub-basin scale eddies such as Batumi and Sevastopol eddies,
595 which are the well-known representatives of vorticity field (Stanev et al. 2000), are also well replicated by the
596 model. Because the transition between summer (less organized) and winter (almost one-gyre) circulation is
597 controlled by the baroclinic eddies (Stanev and Staneva 2000), the present simulation by SCHISM that resolves well
598 the eddy variability has a potential to successfully treat these basic aspects of seasonal evolution.

599 The patterns of sea surface shown every 5th day agree well with earlier numerical simulations using structured-grid
600 models (Stanev 2005). The number of coastal anticyclones of about 8 compares well with the number of observed
601 ones, which is derived from the statistics using SSALTO/ DUACS data product
602 ([http://www.aviso.altimetry.fr/en/data/product-information/information-about-mono-and-multi-mission-
603 processing/ssaltoduacs-multimission-altimeter-products.html](http://www.aviso.altimetry.fr/en/data/product-information/information-about-mono-and-multi-mission-processing/ssaltoduacs-multimission-altimeter-products.html); last accessed Jan 29, 2016). Similarly to those
604 previous results, the meandering activity is especially intense near steeper slopes, e.g. in the northern, eastern and
605 southern coasts. The loop current and eastern and western gyres in the middle of the basin are clearly visible.

606 The model’s ability to resolve the baroclinic instability is contrasted below with SELFE results using the same initial
607 data and forcing, and a similar horizontal and vertical resolution (21S+30Z layers) (Fig. 16b); the SELFE results
608 represented the best we were able to obtain from this model. There are apparent similarities between the two models:
609 the shape of the cyclonic gyre in the middle is similar, and the contrast of sea levels between coastal and open sea is
610 comparable, although the eddy-resolving SCHISM simulation shows a steeper sea-surface slope. The performance
611 of the two models in the area of the shallow Azov Sea, where the process is mostly driven by propagating
612 atmospheric disturbances and dominated by friction, is also similar. However a number of major differences
613 between the two models are apparent, and the most pronounced among them is the clockwise circulation in the
614 eastern-most part of the Black Sea predicted by SELFE versus the formation of an eddy dipole in SCHISM. SELFE
615 is also not in a position to adequately simulate the counter-current along the west coast, which is commonly
616 observed in this area; the well-known Sebastopol eddy is totally missing in this model as well. A number of smaller
617 eddies in the north and south coasts are also successfully captured by SCHISM but not by SELFE. The smoother
618 SSH produced by SELFE is mostly a symptom of the larger dissipation inherent in the model, although the lack of
619 LSC² grid therein is also partially responsible (SCHISM results with the same SZ grid indicate only mild
620 degradation of model skill; not shown). Since SELFE does not have implicit TVD² solver, its efficiency for this case
621 is similar to SCHISM with the explicit TVD method.

622 Differences in the surface heights associated with these eddies between SELFE and SCHISM are 5-10 cm, which is
623 comparable to the anomalies caused by eddies (Stanev et al. 2000). Therefore we conclude that SELFE filters out
624 baroclinic instability, especially eddies with diameter of about 100 km, which are the characteristic scales of eddies
625 seen in altimeter, drifter and color data (Ozsoy et al. 1993; Stanev 2005). The meanders predicted by SCHISM on

626 the Rim Current propagate with a speed of about 20 cm/s, and in some specific areas, such as the area east of
627 Sakarya Canyon (29-31 E), the propagation speed often exceeds 1 m/s. These are also consistent with the
628 observations (Ozsoy et al. 1993).

629 **5.4 Outlook: from creek to ocean**

630 The satisfactory performance of SCHISM in the eddying regime as demonstrated in the previous test cases, and in
631 the non-eddying regime as demonstrated previously, makes it potentially capable of seamlessly simulating processes
632 from deep ocean to shallow environment in estuaries, rivers, creeks and lakes. We remark that the time step we used
633 for the realistic field case of Black Sea, North Sea-Baltic Sea (Zhang et al. 2016) and Kuroshio (Zhang et al. 2015)
634 falls in the same range as that for the non-eddying regime, i.e. 100-200sec, and therefore a single time step can be
635 used for cross-scale applications. Our experience so far demonstrates that as long as one pays attention to smooth
636 transition of grid resolution from eddying to non-eddying regimes, and adds back some numerical dissipation in the
637 non-eddying regime (e.g. via a larger viscosity locally or filter), SCHISM is capable of simulating creek-to-ocean
638 system as a whole without the need for grid nesting. Demonstration of such a seamless capability is on-going for
639 BS-TSS, South and East China Seas, and US east coast and will be reported in upcoming publications.

640

641 **6. Conclusions**

642 We have developed a new cross-scale unstructured-grid model (SCHISM) by revamping key formulations in an
643 older model (SELFE). Major revisions include: (1) a new implicit transport solver (TVD²) using 2 limiter functions
644 (in space and in time), which has been demonstrated to be accurate and efficient for a wide range of Courant
645 numbers; (2) a new horizontal viscosity formulation for generic unstructured grids; (3) a new higher-order scheme
646 for momentum advection coupled with an iterative smoother to reduce excess mass; (4) addition of quad elements,
647 which in conjunction with the flexible vertical grid system used in SCHISM leads to an advantageous polymorphism
648 (with 1D/2DV/2DH/3D cells being unified in a single model grid).

649 These new revisions prove crucial in SCHISM's capability in successfully simulating processes in the eddying
650 regime, as demonstrated by the results from the 2 challenging test cases, mainly due to the much reduced numerical
651 dissipation and enhanced efficiency. Recently the seamless cross-scale capability of SCHISM has also been
652 successfully tested with several other applications..

653 Ongoing work focuses on some transitional issues between eddying and non-eddying regimes as well as enabling
654 variable resolution in the eddying regime. Our and other's experience (Danilov, private communication) suggests
655 that numerical schemes designed for eddying regime may not be ideal for non-eddying regime, and therefore
656 transition of schemes might be desirable. In our case, the combination of MB-LI and MA-KR3 holds most promise,
657 as the latter is ideal for shallow and inundation processes.

658

659 **Acknowledgements**

660 The first author thanks Dr. Sergey Danilov for many enlightening discussions on the subject of eddying regime. Part
661 of this work was accomplished during the 1st author's tenure as a HWK Fellow and financial support by Hanse-
662 Wissenschaftskolleg (HWK, Germany) is gratefully acknowledged. S. Grashorn is funded by the initiative Earth
663 Science Knowledge Platform (ESKP) operated by the Helmholtz Association. Simulations shown in this paper were
664 conducted on the following HPC resources: (1) Sciclone at the College of William and Mary which were provided
665 with the assistance of the National Science Foundation, the Virginia Port Authority, and Virginia's Commonwealth
666 Technology Research Fund; (2) the Extreme Science and Engineering Discovery Environment (XSEDE; Grant TG-
667 OCE130032), which is supported by National Science Foundation grant number OCI-1053575; (3) NASA's
668 Pleiades. The authors thank the comments made by 3 anonymous reviewers which made the paper stronger.

669

670 **Figure captions**

671 Fig. 1: SCHISM modelling system. The modules that are linked by arrows can exchange internal data directly
672 without going through the hydrodynamic core in the center.

673 Fig. 2: Staggering of variables in SELFE/SCHISM. The elevation is defined at node (vertex) of a triangular element,
674 horizontal velocity at side center and whole levels, vertical velocity at element centroid and whole level, and tracers

675 at the prism center. The variable arrangement on a quad prism in SCHISM is similar. The top and bottom faces of
676 the prism may not be horizontal, but the other 3 faces are always vertical.

677 Fig. 3: Two steps in Eulerian-Lagrangian method. (a) The characteristic equation (6) is integrated backward in
678 space and time, starting from a side center (the green dot). The characteristic line is further subdivided into smaller
679 intervals (bounded by the red dots), based on local flow gradients, and a 2nd-order Runge-Kutta method is used
680 within each interval. The foot of characteristic line is marked as a yellow dot. Note that the vertical position of the
681 trajectory is also changing and so the tracking is in 3D space. (b) Interpolation is carried out at FOCL (yellow dot),
682 based on either the nodes of the containing elements (blue dots), or the 2-tier neighborhood (blue plus red dots; the
683 latter are the neighbors of the blue dots) using a dual kriging method. Proper linear vertical interpolation has been
684 carried out first to bring the values at each node onto a horizontal plane before the horizontal interpolation is done.

685 Fig. 4: Two methods of converting side velocities to a node velocity. (a) Inverse distance interpolation from sides
686 (blue dots) to node (yellow dot); (b) use of FEM shape function to find the node velocity within each element first
687 (the red arrow), i.e. $\mathbf{u}_i = \mathbf{u}_{II} + \mathbf{u}_{III} - \mathbf{u}_I$, followed by a simple averaging method to calculate the final value from all of its
688 surrounding elements (dashed arrows).

689 Fig. 5: Shapiro filters for (a) triangular and (b) quadrangular elements. The same stencils are used to construct the
690 viscosity. 'P' and 'II' are 2 adjacent elements of side of interest ('0'). The extended stencil used in constructing bi-
691 harmonic viscosity is shown in (c). The special case of a boundary side is shown in (d).

692 Fig. 6: Temperature after 1 rotation in the rotating Gauss hill test from various schemes with $\Delta x = 50\text{m}$. ELAD filter
693 is applied to all 'KR' schemes.

694 Fig. 7: Convergence curves of various advection schemes. The equations in each panel are linear regression fit. The
695 intersection with x -axis in each equation is related to the coefficient of leading-order truncation error, and MB-LI
696 has the smallest value.

697 Fig. 8: Model polymorphism illustrated with a toy problem. The mixed triangular-quadrangular grid and the
698 bathymetry are shown in the foreground. The vertical transect grid along the redline going from deep ocean into
699 estuary ('shipping channel') is shown in insert (a). The 3D view of the grid near the head of estuary is shown in
700 insert (b), with few layers on the shallow shoals. The grid near the upstream river is shown in insert (c), where
701 transition from 2DV to 1D grid can be seen. In the test, a M2 tide is applied at the ocean boundary, and fresh water
702 discharges are imposed at the heads of the river and estuary.

703 Fig. 9: Snapshot of velocity (a&c) and salinity (b&d) along the river transect (cf. Fig. 8c) showing the transition
704 from 2DV to 1D region (i.e. the flat portion on the left). (a&b) correspond to a peak flood and (c&d) a peak ebb. The
705 uni-directional river flow can be seen even during flood, and the tilt of isohaline line in (b) into the 1D zone is due to
706 the linear interpolation of colors used in plotting; otherwise the 1D zone shows a uniform salinity/velocity along the
707 vertical column. The burgundy line in (a&c) is the bottom.

708 Fig. 10: Vertical transects of temperature at $t=17$ hours, with $\Delta t=200\text{s}$ and vertical resolution of 10, 5, 2 and 1m in
709 (a-d), and two different time steps (e&f). The horizontal resolution is fixed at 500m.

710 Fig. 11: Time history of front location from (a) different vertical resolution (with horizontal resolution fixed at
711 500m); (b) different horizontal resolution (with vertical resolution fixed at 1m). The time step is fixed at 200s. The
712 theoretical results of Benjamin (1968) are also shown.

713 Fig. 12: Simulated mean kinetic energy (doubled kinetic energy scaled by mass) over time.

714 Fig. 13: Snapshot of SSH for the entire grid showing periodicity along the zonal band.

715 Fig. 14: Snapshot of (a) SSH, (b) temperature at 100m depth, and (c) relative vorticity (scaled by local Coriolis
716 parameter) at 100m depth.

717 Fig. 15: (a) Black Sea bathymetry. Also shown are major geographic names and rivers around Black Sea (Sakarya,
718 Kizilirmak, Rioni, Dniepr, Dniestr, and Danube) and Azov Sea (Don and Kubon). (b) Bottom slope
719 $(\sqrt{(\partial h/\partial x)^2 + (\partial h/\partial y)^2})$ of Black Sea, with values larger than 0.05 (1:20) being highlighted. (c) Hannah-Wright
720 ratios, with values larger than 0.1 being highlighted. (d) SCHISM grid for Black Sea showing the placement of
721 nodes. Uniform resolution of 3km is used except near the exit to Bosphorus Strait.

722 Fig. 16: Snapshots of SSH from (a) SCHISM; (b) SELFE. The time stamps are shown near the top of each panel.
723 Major eddies in Black Sea can be seen in (a) and compared with Stanev (2005).

724

725 REFERENCES

726 Arakawa, A. and V.R. Lamb (1977) Computational design of the basic dynamical processes of the UCLA general
727 circulation model, *Methods of Computational Physics* 17. New York: Academic Press. pp. 173–265.

728 Azevedo, A., Oliveira, A., Fortunato, A.B., Zhang, Y. and A.M. Baptista (2014) A cross-scale numerical modeling
729 system for management support of oil spill accidents, *Marine Pollution Bulletin*, 80, 132-147.

730 Benjamin, T.B. (1968) Gravity currents and related phenomena. *J. Fluid Mech.* 31, 209–248.

731 Bertin, X., Li, K., Roland, A., Zhang, Y., Breilh, J.F. and E. Chaumillon (2014), A modeling-based analysis of the
732 flooding associated with Xynthia, central Bay of Biscay, *Ocean Eng.* 94, 80-89.

733 Burla, M., Baptista, A.M. Zhang, Y., and S. Frolov (2010), Seasonal and inter-annual variability of the Columbia
734 River plume: a perspective enabled by multi-year simulation databases. *Journal of Geophysical Research: special*
735 *issue on NSF RISE project*, 115, C00B16.

736 Casulli, V. and E. Cattani (1994), Stability, accuracy and efficiency of a semiimplicit method for 3D shallow water
737 flow, *Comput. Math. Appl.*, 27, 99–112.

738 Casulli, V. and P. Zanolli (2005), High resolution methods for multidimensional advection–diffusion problems in
739 free-surface hydrodynamics, *Ocean Model.*, 10, 137–151.

740 Cerco, C. and T. Cole (1993), Three-Dimensional Eutrophication Model of Chesapeake Bay. *J. Environ. Eng.*,
741 119(6), 1006–1025.

742 Chai, F., Dugdale, R.C., Peng, T-H, Wilkerson, F.P. and R. T. Barber (2002), One Dimensional Ecosystem Model of
743 the Equatorial Pacific Upwelling System, Part I: Model Development and Silicon and Nitrogen Cycle. *Deep-Sea Res.*
744 *II.* 49(13-14), 2713-2745.

745 Comblen, R., Legrand, S., Deleersnijder E., and V. Legat (2009), A finite element method for solving the shallow
746 water equations on the sphere. *Ocean Modelling*, 28, 12-23.

747 Cotter, C.J., Ham, D.A. (2011) Numerical wave propagation for the triangular P1DG-P2 finite element pair, *J.*
748 *Comput. Phys.*, 230, 2806-2820.

749 Danilov, S. (2012), Two finite-volume unstructured mesh models for large-scale ocean modeling, *Ocean Modelling*
750 47, 14–25.

751 Danilov, S. and A. Androsov (2015), Cell-vertex discretization of shallow water equations on mixed unstructured
752 meshes, *Ocean Dyn.* 65, 33–47.

753 Danilov, S. and Q. Wang (2015), Resolving eddies by local mesh refinement, *Ocean Modelling*, 93, 75-83.

754 Danilov, S. and Q. Wang (private communication) Resolving eddies by local mesh refinement.

755 Dodet, G. (2013), Morphodynamic modelling of a wave-dominated tidal inlet: the Albufeira Lagoon, Ph.D. thesis,
756 Univ. La Rochelle (France).

757 Duraisamy, K. and J.D. Baeder (2007), Implicit Scheme For Hyperbolic Conservation Laws Using Nonoscillatory
758 Reconstruction In Space And Time, *Siam J. Sci. Comput.* 29(6), 2607–2620.

759 Griffies, S.M. and R.W. Hallberg (2000), Biharmonic Friction with a Smagorinsky-Like Viscosity for Use in Large-
760 Scale Eddy-Permitting Ocean Models, *Monthly Weather Review*, 128, 2935-46.

761 Gravel, S. and A. Staniforth (1994), A mass-conserving semi-Lagrangian scheme for the shallow-water equations,
762 *Mon. Wea. Rev.*, 122, 243-248.

763 Ham, D.A., Pietrzak, J., and G.S. Stelling (2006), A streamline tracking algorithm for semi-Lagrangian advection
764 schemes based on the analytic integration of the velocity field, *Journal of Computational and Applied Mathematics*
765 192, 168–174.

- 766 Ham, D.A., Kramer, S.C., Stelling, G.S., and J. Pietrzak (2007), The symmetry and stability of unstructured mesh C-
767 grid shallow water models under the influence of Coriolis, *Ocean Modelling* 16, 47–60.
- 768 Haney, R.L. (1991) On the pressure gradient force over steep topography in sigma coordinate ocean models, J.
769 *Phys. Oceanogr.*, 21, 610–619.
- 770 Hannah C. G., and D. G. Wright (1995), Depth dependent analytical and numerical solutions for wind-driven flow
771 in the coastal ocean, *Quantitative Skill Assessment for Coastal Ocean Models*. D. R. Lynch and A. M. Davies (Ed.),
772 A.G.U. 47, 125-152.
- 773 Ilicak, M., Adcroft, A.J., Griffies, S. M., and R.W. Hallberg (2012), Spurious dianeutral mixing and the role of
774 momentum closure. *Ocean Modelling*, 45-46(0):37-58.
- 775 Le Roux, D.Y., Lin, C.A., Staniforth, A. (1997), An accurate interpolating scheme for semi-Lagrangian advection
776 on an unstructured mesh for ocean modelling, *Tellus*, 49A, 119–138.
- 777 Le Roux, D.Y., Sène, A., Rostand, V., and E. Hanert (2005), On some spurious mode issues in shallow-water
778 models using a linear algebra approach. *Ocean Modelling* 10, 83–94.
- 779 Le Roux, D.Y. (2012) Spurious inertial oscillations in shallow-water models, *J. Comput. Phys.* 231, 7959-7987.
- 780 IOC, IHO and BODC (2003), Centenary Edition of the GEBCO Digital Atlas, published on CD-ROM on behalf of
781 the Intergovernmental Oceanographic Commission and the International Hydrographic Organization as part of the
782 General Bathymetric Chart of the Oceans, British Oceanographic Data Centre, Liverpool, U.K.
- 783 Özsoy E., Ünlüata Ü. and Top Z. (1993), The evolution of Mediterranean water in the Black Sea: interior mixing
784 and material transport by double diffusive intrusions. *Progress In Oceanography*, 31, 3, 275–320.
- 785 Özsoy, E. and Ü. Ünlüata (1997), Oceanography of the Black Sea: A Review of Some Recent Results, *Earth Sci.*
786 *Rev.*, 42(4), 231-272.
- 787 Persson, P. and G. Strang, (2004) A Simple Mesh Generator in MATLAB, *SIAM Review*, 46(2), 329-345.
- 788 Pinto, L., Fortunato, A.B., Zhang, Y., Oliveira, A. and F.E.P.Sancho (2012), Development and validation of a three-
789 dimensional morphodynamic modelling system, *Ocean Modelling*, 57-58, 1-14.
- 790 Ringler, T.D., Thuburn, J., Klemp, J.B., and W.C. Skamarock (2010), A unified approach to energy conservation
791 and potential vorticity dynamics for arbitrarily-structured C-grids, *J. Comput. Phys.* 229, 3065–3090.
- 792 Rodrigues M., A. Oliveira, H. Queiroga, A.B. Fortunato, and Y. Zhang (2009), Three-dimensional modeling of the
793 lower trophic levels in the Ria de Aveiro (Portugal), *Ecological Modelling*, 220(9-10), 1274-1290.
- 794 Roland, A., Zhang, Y., Wang, H.V., Meng, Y., Teng, Y., Maderich, V., Brovchenko, I., Dutour-Sikiric, M. and U.
795 Zanke (2012), A fully coupled wave-current model on unstructured grids, *Journal of Geophysical Research-*
796 *Oceans*,117,C00J33,doi:10.1029/2012JC007952.
- 797 Shapiro, R. (1970), Smoothing, filtering and boundary effects, *Rev. Geophys. Space Phys.* 8 (2), 359–387.
- 798 Shchepetkin, A.F. and J.C. McWilliams (1998), Quasi-Monotone Advection Schemes Based on Explicit Locally
799 Adaptive Dissipation , *Monthly Weather Review*, 126, 1541-80.
- 800 Shen, J. and L. Haas (2004) Calculating age and residence time in the tidal York River using three-dimensional
801 model experiments, *Estuarine, Coastal and Shelf Science*, 61, 449–461.
- 802 Stanev, E.V. and J.V. Staneva (2000), The impact of the baroclinic eddies and basin oscillations on the transitions
803 between different quasi-stable states of the Black Sea circulation, *Journal of Marine Systems* 24:3-26.
- 804 Stanev, E.V., Le Traon, P.-Y., E.L., Peneva (2000), Sea level variations and their dependency on meteorological and
805 hydrological forcing. Analysis of altimeter and surface data for the Black Sea. *J. Geophys. Res.*, vol. 105 (C7),
806 17203–17216.
- 807 Stanev, E.V, and E.L. Peneva (2002), Regional sea level response to global climatic change: Black Sea examples,
808 *Glob Planet Change*, 32, 33–47

- 809 Stanev, E.V. (2005), Understanding Black Sea Dynamics: Overview of recent numerical modelling. *Oceanography*,
810 18 (2), 52–71.
- 811 Stanev, E.V. and X. Lu (2013), European semi-enclosed seas: basic physical processes and their numerical
812 modelling. In: Soomere,T., Quak,E.(Eds.), Preventive methods for coastal protection. Springer, Switzerland,
813 pp.131–179. doi:10.1007/978-3-319-00440-2_5.
- 814 Stanev, E.V., Grashorn, S. and Y. Zhang (in preparation) Cascading estuaries: Numerical simulations of the Inter-
815 basin exchange in the coupled Azov-Black-Marmara-Mediterranean Seas system, *Ocean Modelling*.
- 816 Umlauf, L. and H. Burchard (2003), A generic length-scale equation for geophysical turbulence models, *J. Mar. Res.*
817 6, 235–265.
- 818 Ye, F., Zhang, Y., Friedrichs, M., Irby, I., Shen, J., Wang, H.V., and Z. Wang (submitted) A 3D baroclinic model of
819 the upper Chesapeake Bay and its tributaries, *Ocean Modelling*.
- 820 Zanke, U.C.E. (2003), On the influence of turbulence on the initiation of sediment motion. *International Journal of*
821 *Sediment Research*, 18(1), 17.
- 822 Zhang, Y., Baptista, A.M., and E.P. Myers (2004), A cross-scale model for 3D baroclinic circulation in estuary–
823 plume–shelf systems: I. Formulation and skill assessment. *Cont. Shelf Res.*, 24, 2187–2214.
- 824 Zhang, Y., and A. M. Baptista (2008), SELFE: A semi-implicit Eulerian–Lagrangian finite-element model for cross-
825 scale ocean circulation, *Ocean Modelling*, 21(3–4), 71-96.
- 826 Zhang, Y., R.C. Witter, and G.R. Priest (2011), Tsunami–tide interaction in 1964 Prince William Sound tsunami,
827 *Ocean Modelling*, 40(3–4), 246-259.
- 828 Zhang, Y., Ateljevich, E., Yu, H-C., Wu, C-H., and J.C.S. Yu (2015), A new vertical coordinate system for a 3D
829 unstructured-grid model, *Ocean Modelling*, 85, 16-31.
- 830 Zhang, Y., Stanev, E.V. and S. Grashorn (2016) Unstructured-grid model for the North Sea and Baltic Sea:
831 validation against observations, *Ocean Modelling*, 97, 91-108.

Figure1

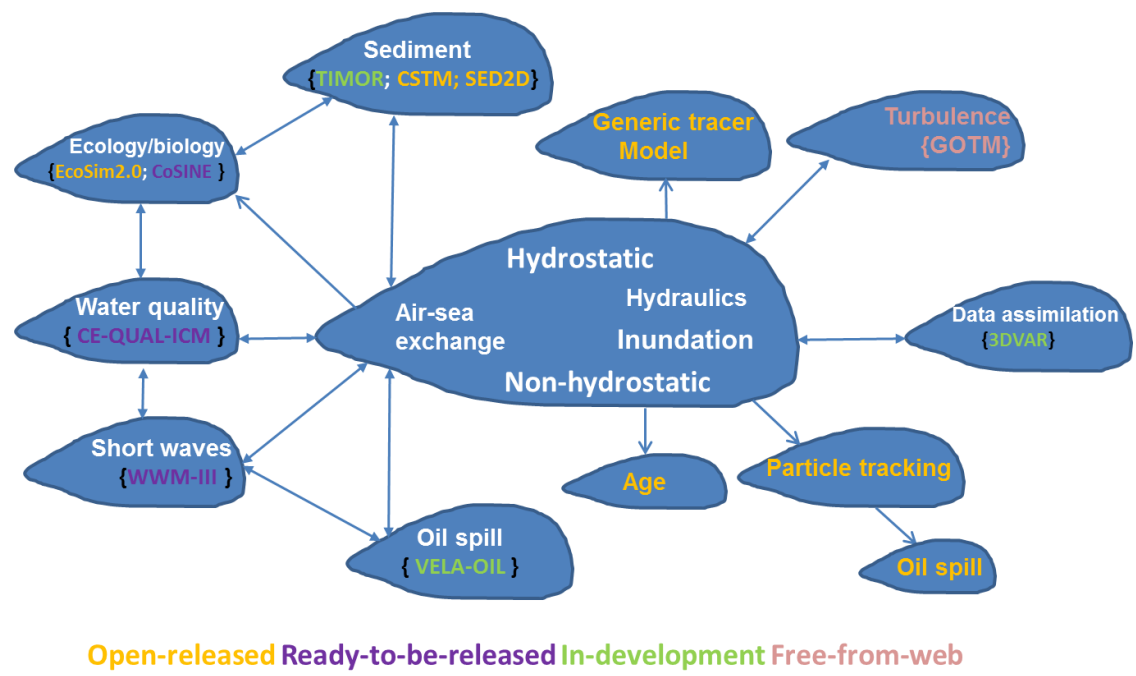


Fig. 1: SCHISM modelling system. The modules that are linked by arrows can exchange internal data directly without going through the hydrodynamic core in the center.

Figure2

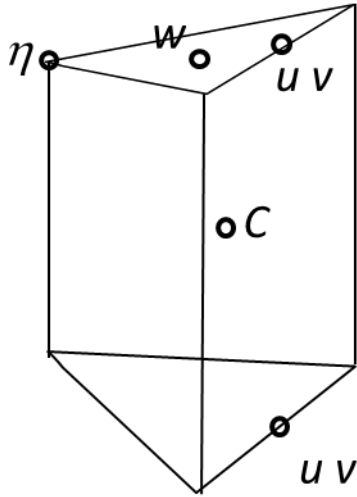


Fig. 2: Staggering of variables in SELFE/SCHISM. The elevation is defined at node (vertex) of a triangular element, horizontal velocity at side center and whole levels, vertical velocity at element centroid and whole level, and tracers at the prism center. The variable arrangement on a quad prism in SCHISM is similar. The top and bottom faces of the prism may not be horizontal, but the other 3 faces are always vertical.

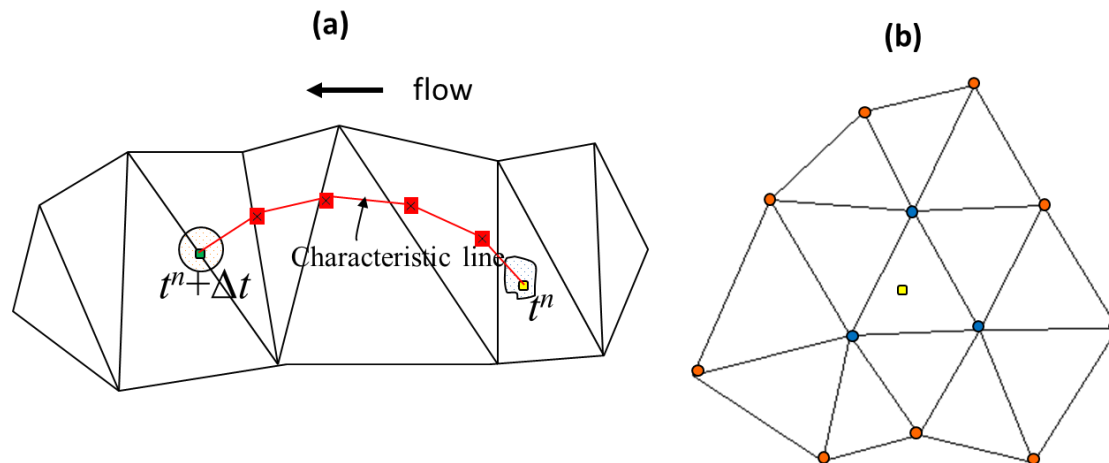


Fig. 3: Two steps in Eulerian-Lagrangian method. (a) The characteristic equation (6) is integrated backward in space and time, starting from a side center (the green dot). The characteristic line is further subdivided into smaller intervals (bounded by the red dots), based on local flow gradients, and a 2nd-order Runge-Kutta method is used within each interval. The foot of characteristic line is marked as a yellow dot. Note that the vertical position of the trajectory is also changing and so the tracking is in 3D space. (b) Interpolation is carried out at FOCL (yellow dot), based on either the nodes of the containing elements (blue dots), or the 2-tier neighborhood (blue plus red dots; the latter are the neighbors of the blue dots) using a dual kriging method. Proper linear vertical interpolation has been carried out first to bring the values at each node onto a horizontal plane before the horizontal interpolation is done.

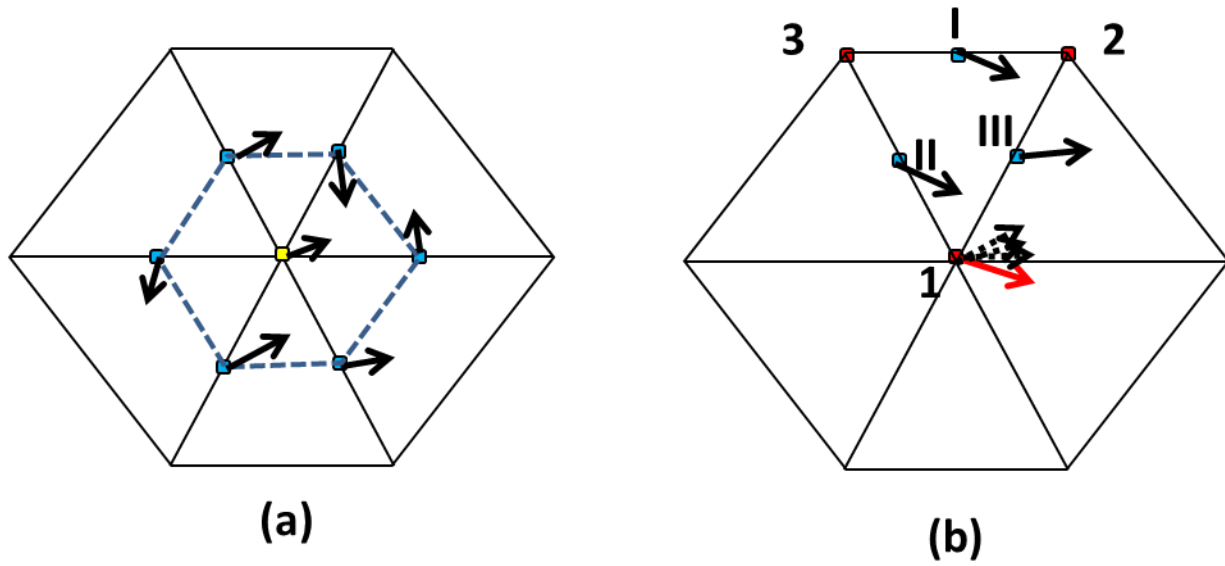


Fig. 4: Two methods of converting side velocities to a node velocity. (a) Inverse distance interpolation from sides (blue dots) to node (yellow dot); (b) use of FEM shape function to find the node velocity within each element first (the red arrow), i.e. $\mathbf{u}_i = \mathbf{u}_{II} + \mathbf{u}_{III} - \mathbf{u}_I$, followed by a simple averaging method to calculate the final value from all of its surrounding elements (dashed arrows).

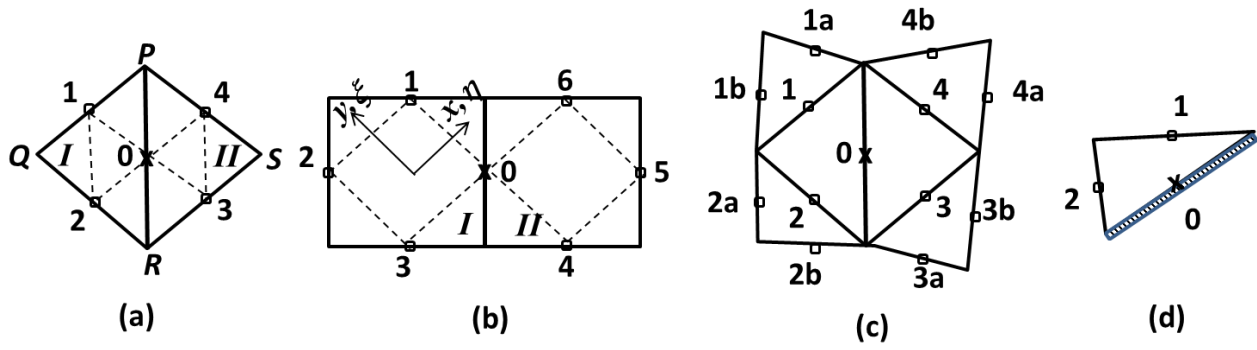


Fig. 5: Shapiro filters for (a) triangular and (b) quadrangular elements. The same stencils are used to construct the viscosity. ' I ' and ' II ' are 2 adjacent elements of side of interest (' 0 '). The extended stencil used in constructing bi-harmonic viscosity is shown in (c). The special case of a boundary side is shown in (d).

Figure6

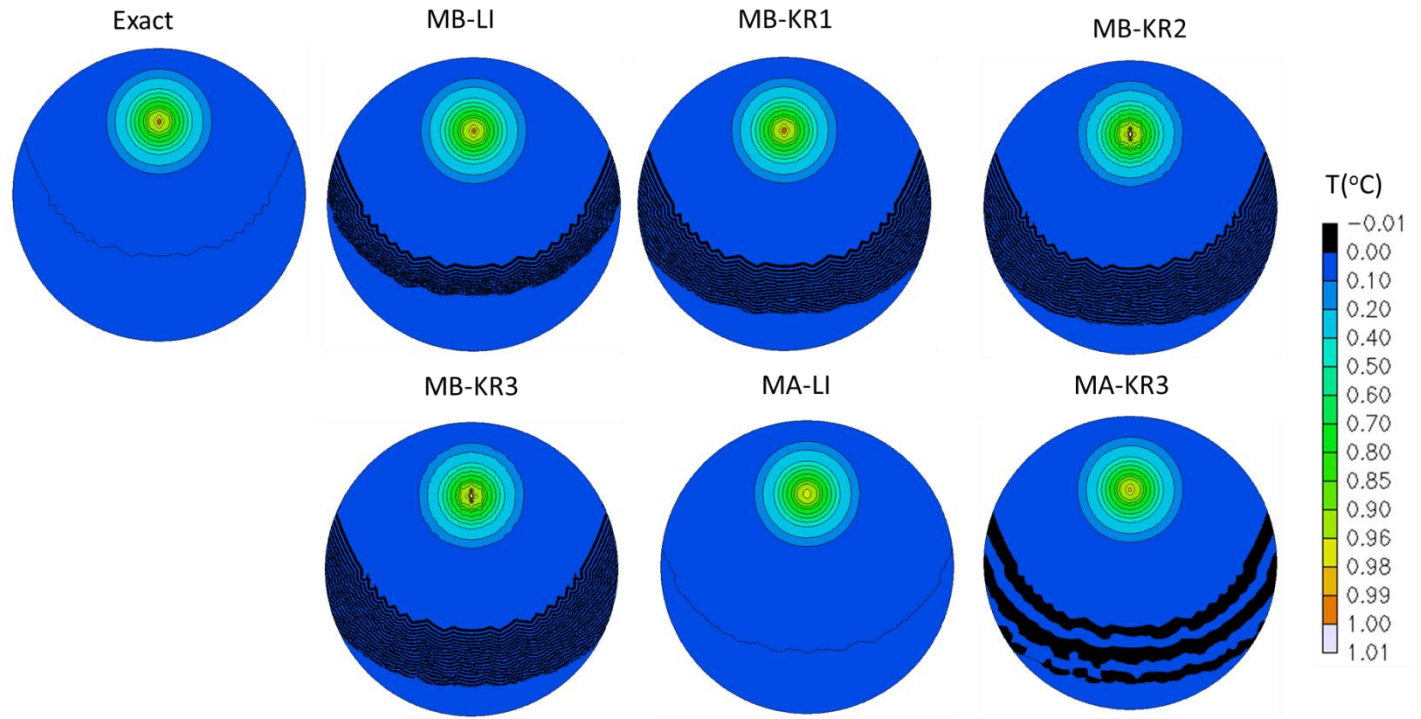


Fig. 6: Temperature after 1 rotation in the rotating Gauss hill test from various schemes with $\Delta x=50m$. ELAD filter is applied to all 'KR' schemes.

Figure7

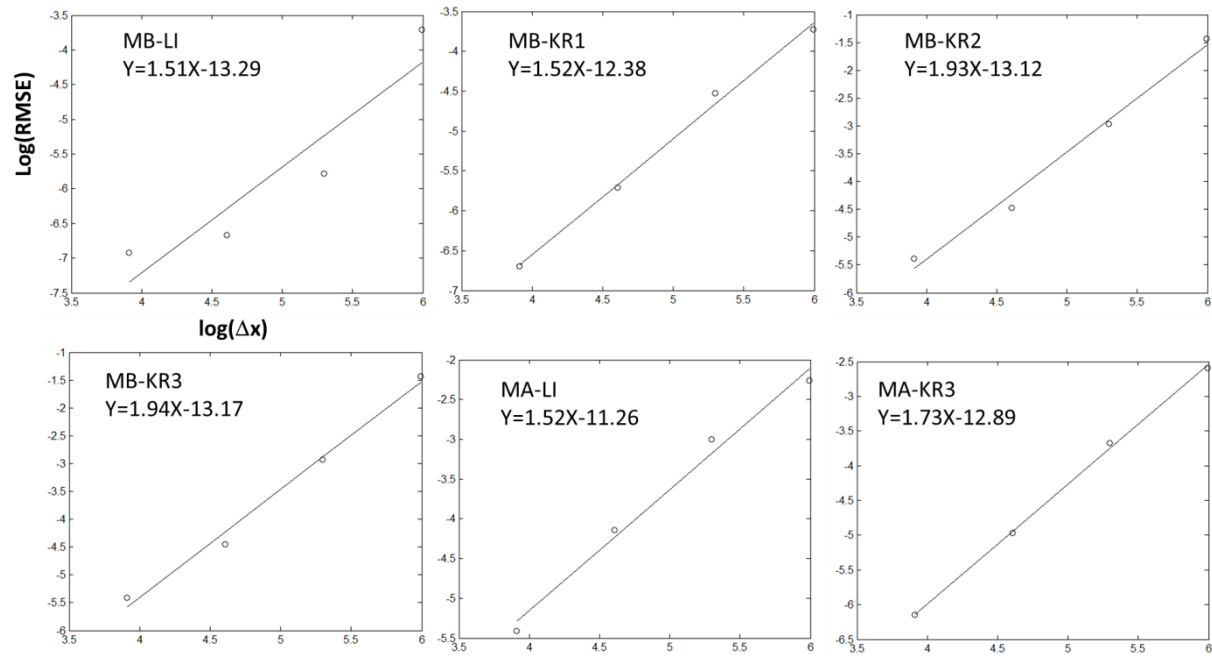


Fig. 7: Convergence curves of various advection schemes. The equations in each panel are linear regression fit. The intersection with x -axis in each equation is related to the coefficient of leading-order truncation error, and MB-LI has the smallest value.

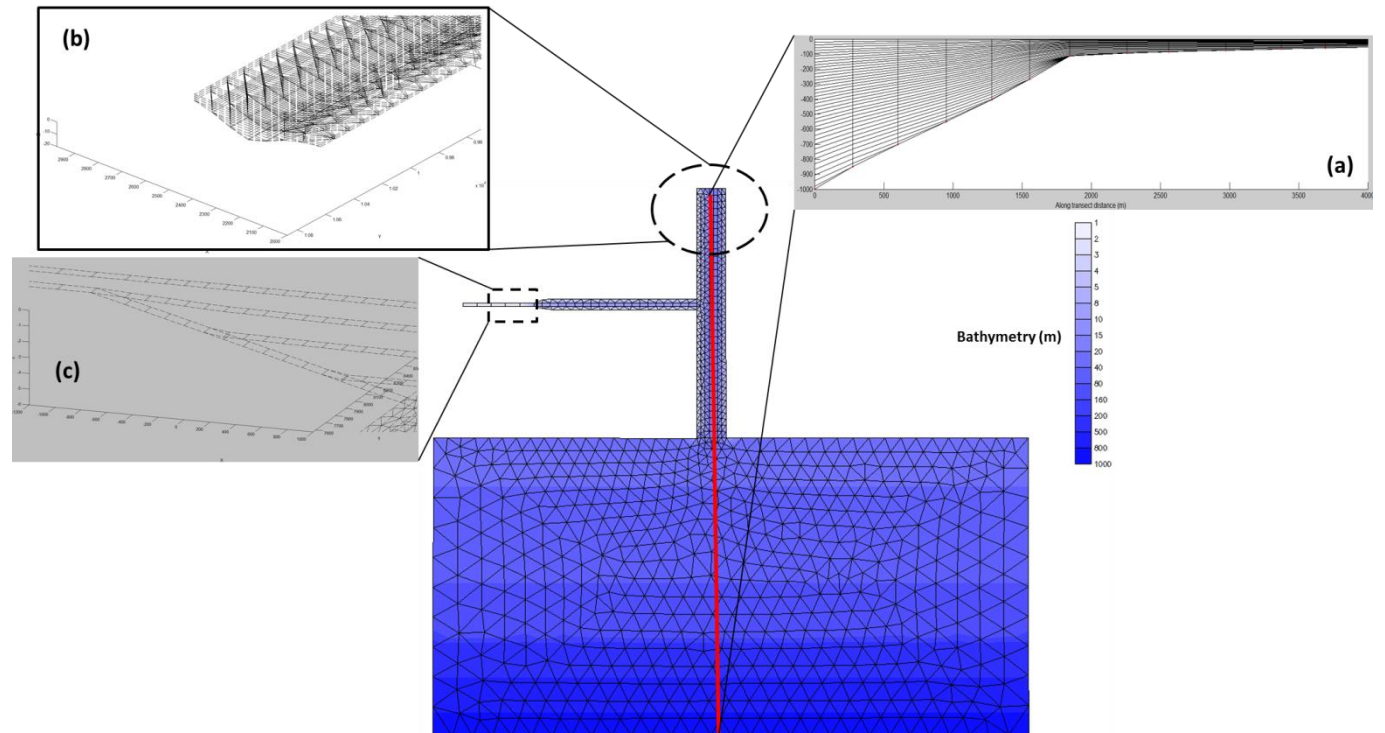


Fig. 8: Model polymorphism illustrated with a toy problem. The mixed triangular-quadrangular grid and the bathymetry are shown in the foreground. The vertical transect grid along the redline going from deep ocean into estuary ('shipping channel') is shown in insert (a). The 3D view of the grid near the head of estuary is shown in insert (b), with few layers on the shallow shoals. The grid near the upstream river is shown in insert (c), where transition from 2DV to 1D grid can be seen. In the test, a M2 tide is applied at the ocean boundary, and fresh water discharges are imposed at the heads of the river and estuary.

Figure9

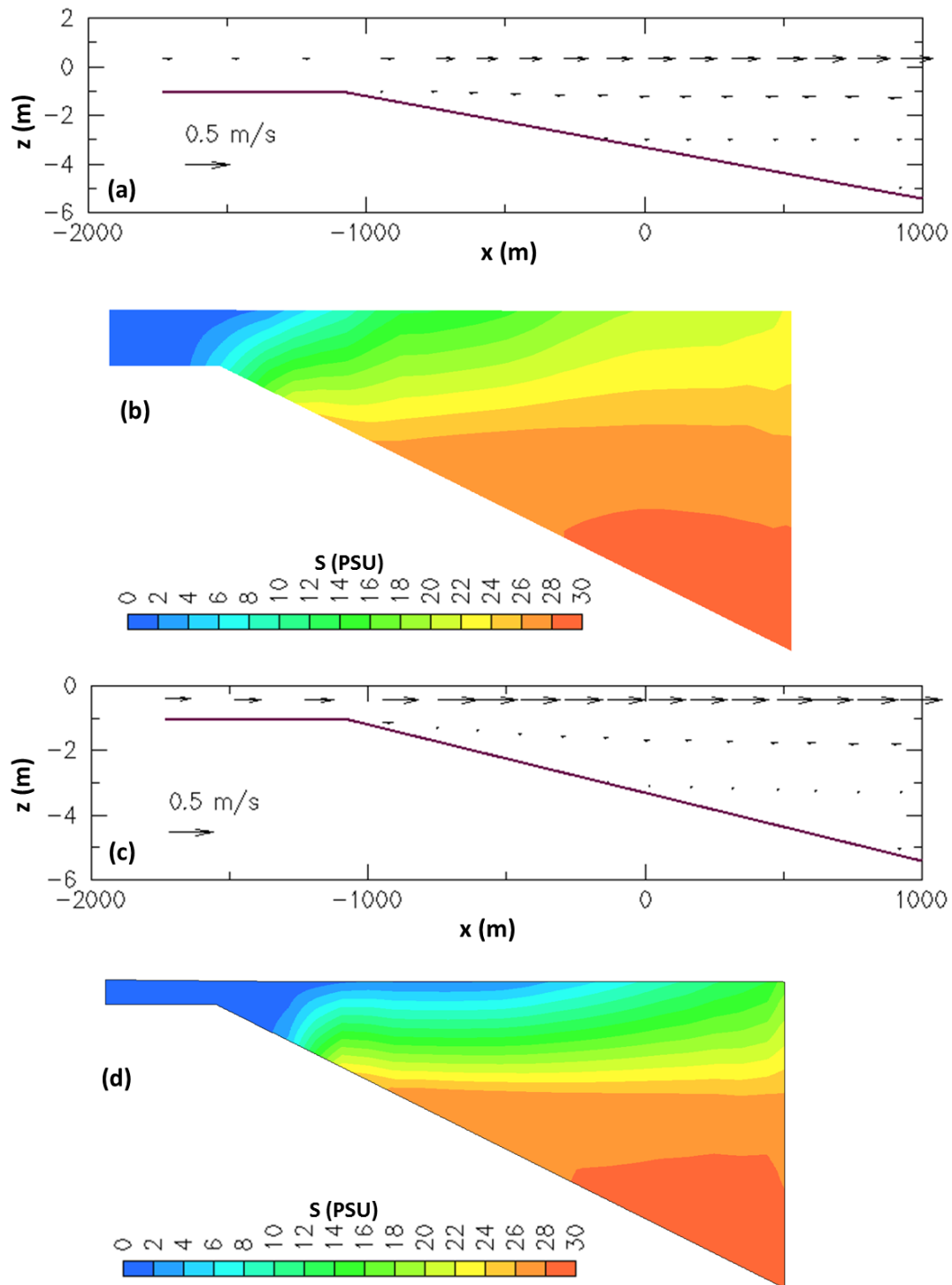


Fig. 9: Snapshot of velocity (a&c) and salinity (b&d) along the river transect (cf. Fig. 8c) showing the transition from 2DV to 1D region (i.e. the flat portion on the left). (a&b) correspond to a peak flood and (c&d) a peak ebb. The uni-directional river flow can be seen even during flood, and the tilt of isohaline line in (b) into the 1D zone is due to the linear interpolation of colors used in plotting; otherwise the 1D zone shows a uniform salinity/velocity along the vertical column. The burgundy line in (a&c) is the bottom.

Figure10

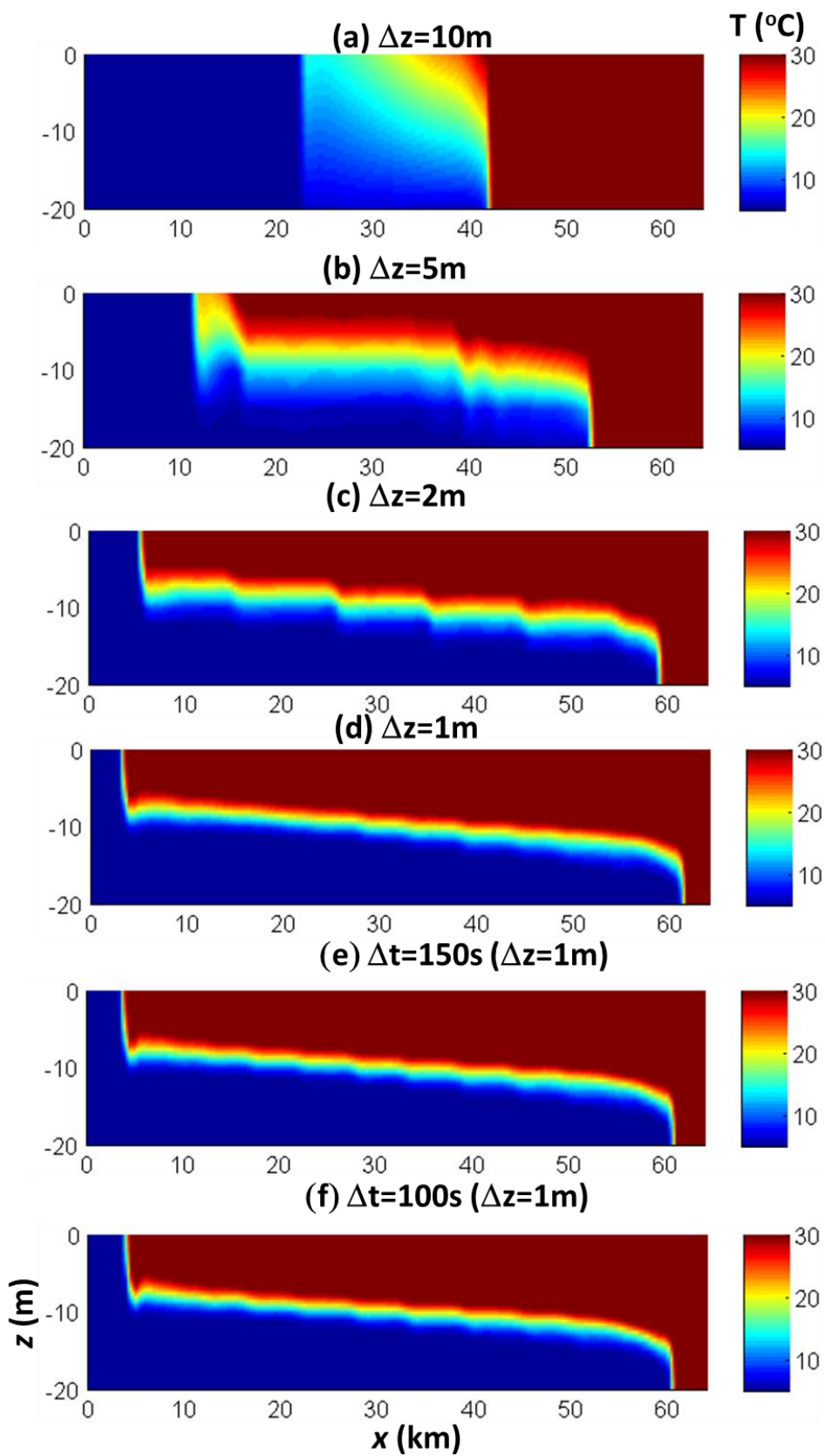


Fig. 10: Vertical transects of temperature at $t=17$ hours, with $\Delta t=200$ s and vertical resolution of 10, 5, 2 and 1m in (a-d), and two different time steps (e&f). The horizontal resolution is fixed at 500m.

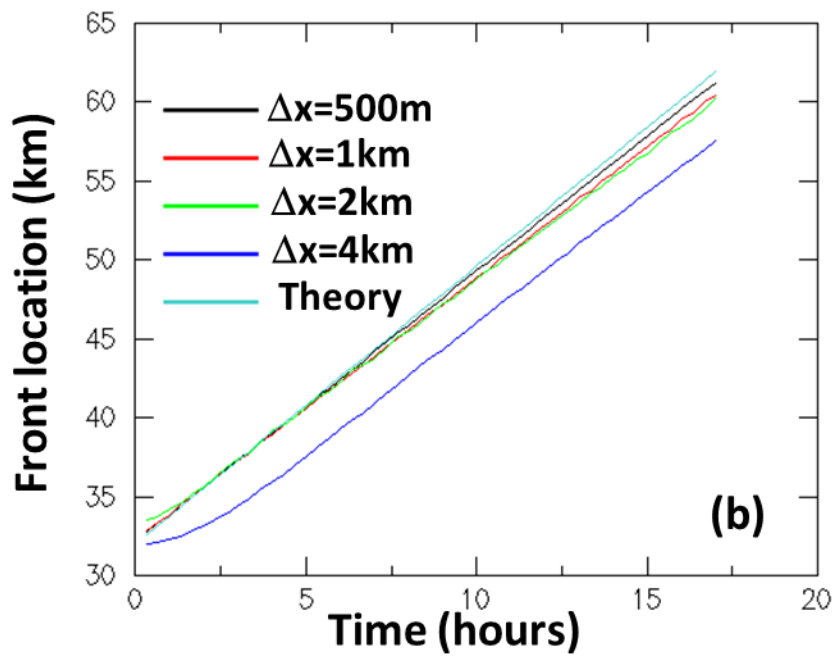
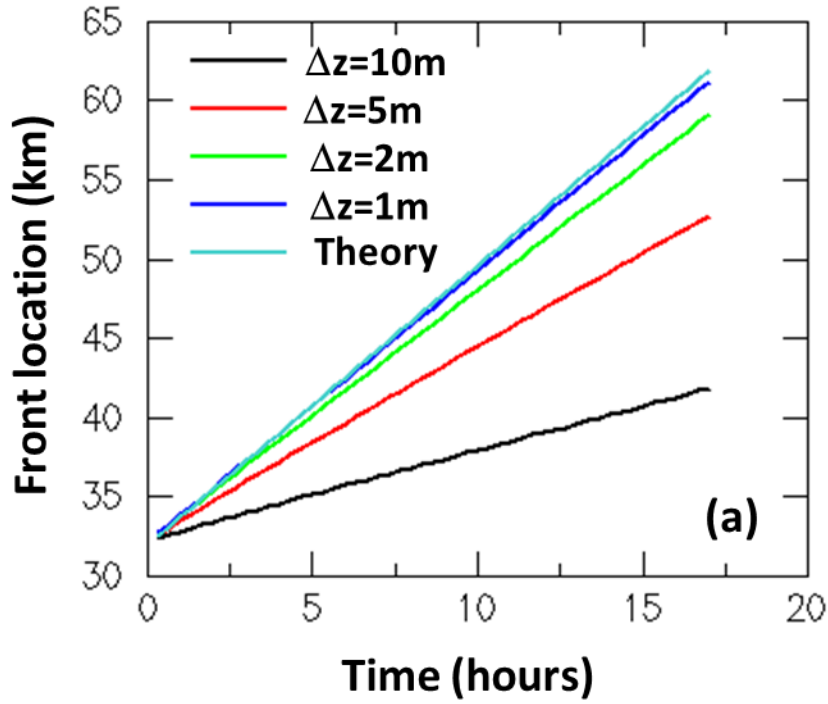


Fig. 11: Time history of front location from (a) different vertical resolution (with horizontal resolution fixed at 500m); (b) different horizontal resolution (with vertical resolution fixed at 1m). The time step is fixed at 200s. The theoretical results of Benjamin (1968) are also shown.

Figure12

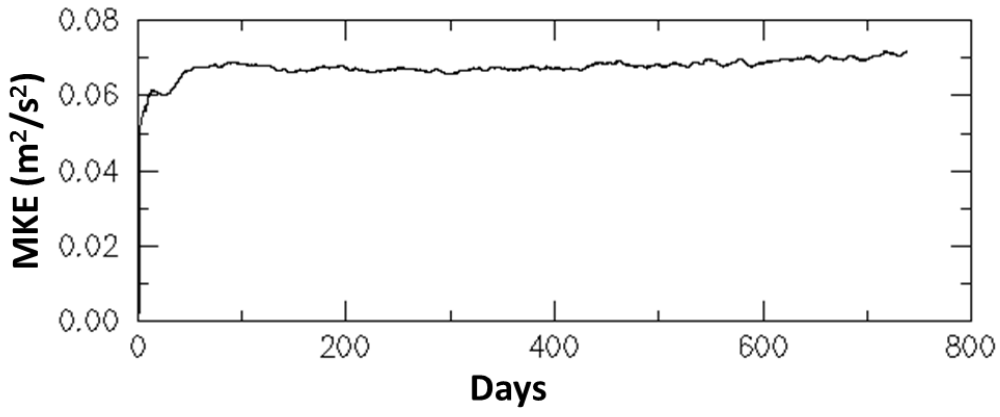


Fig. 12: Simulated mean kinetic energy (doubled kinetic energy scaled by mass) over time.

Figure13

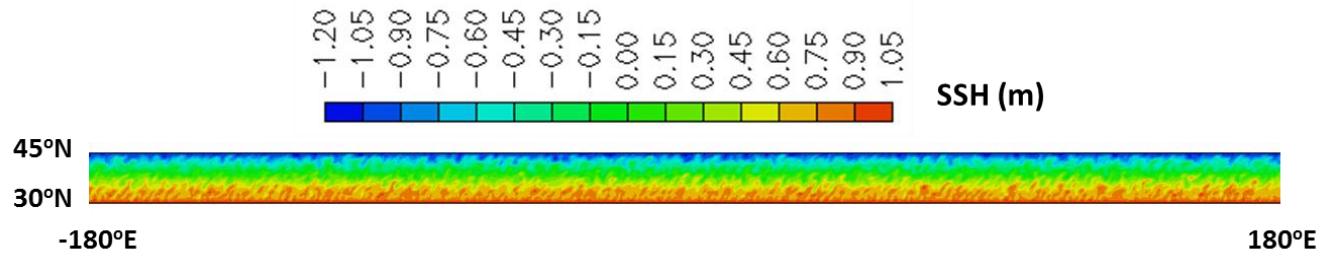
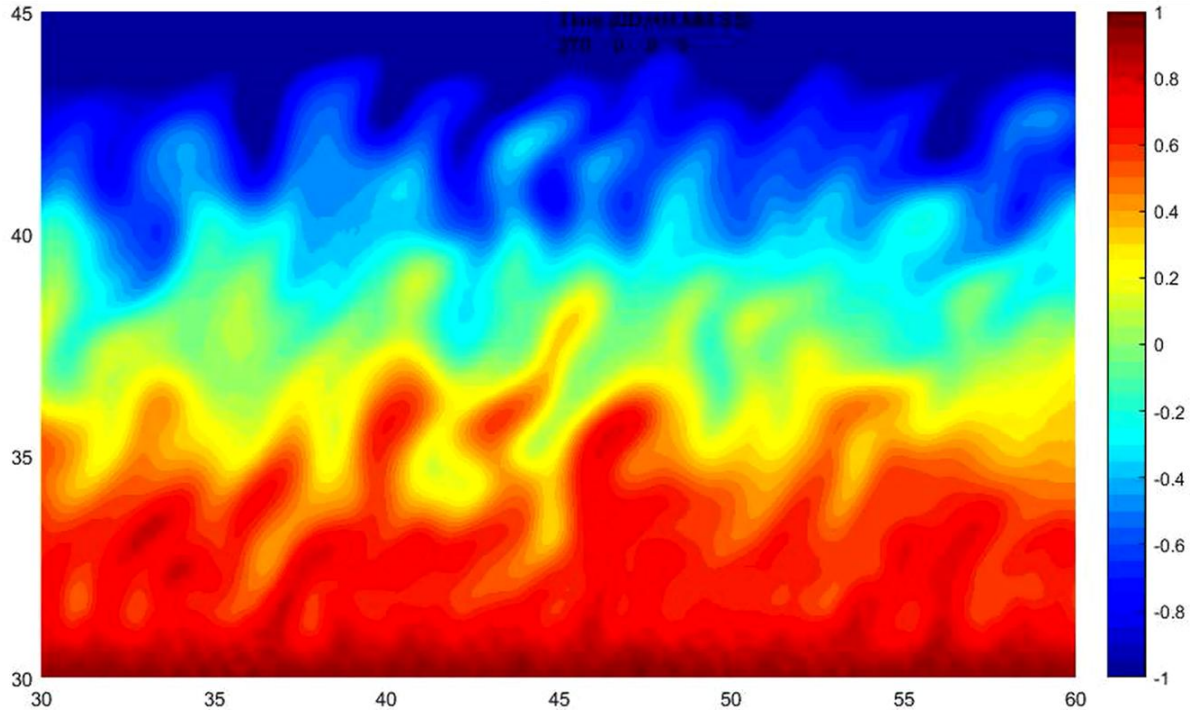


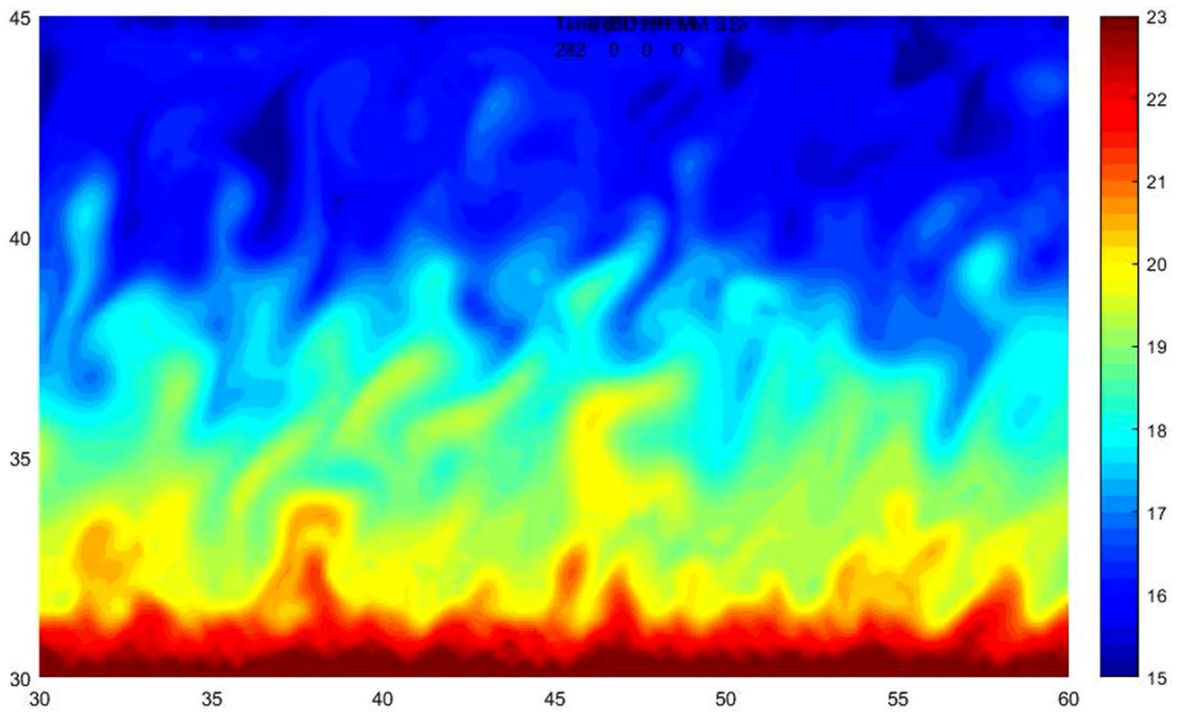
Fig. 13: Snapshot of SSH for the entire grid showing periodicity along the zonal band.

Figure14

(a) SSH (m)



(b) Temperature (°C)



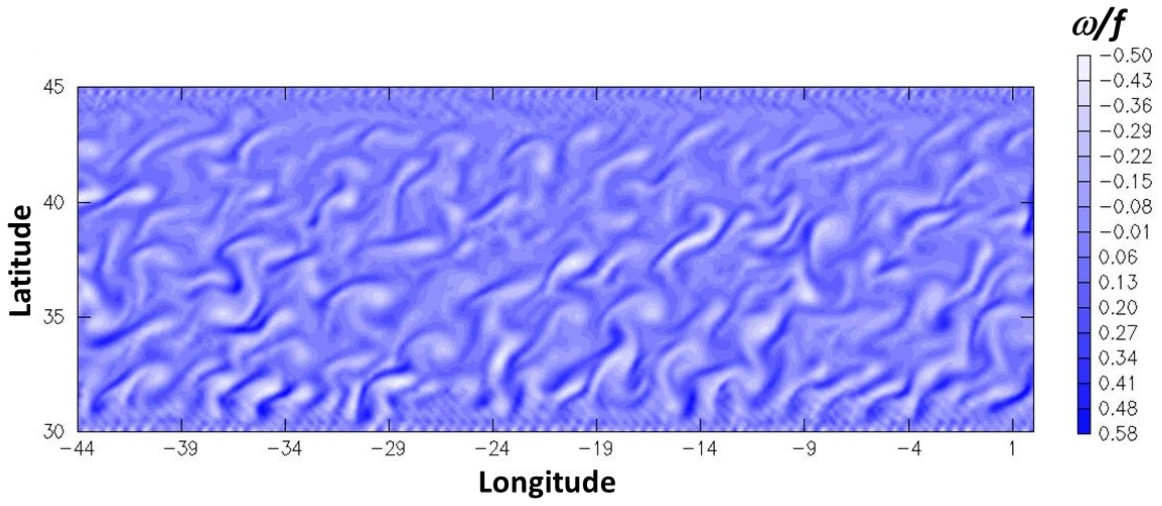
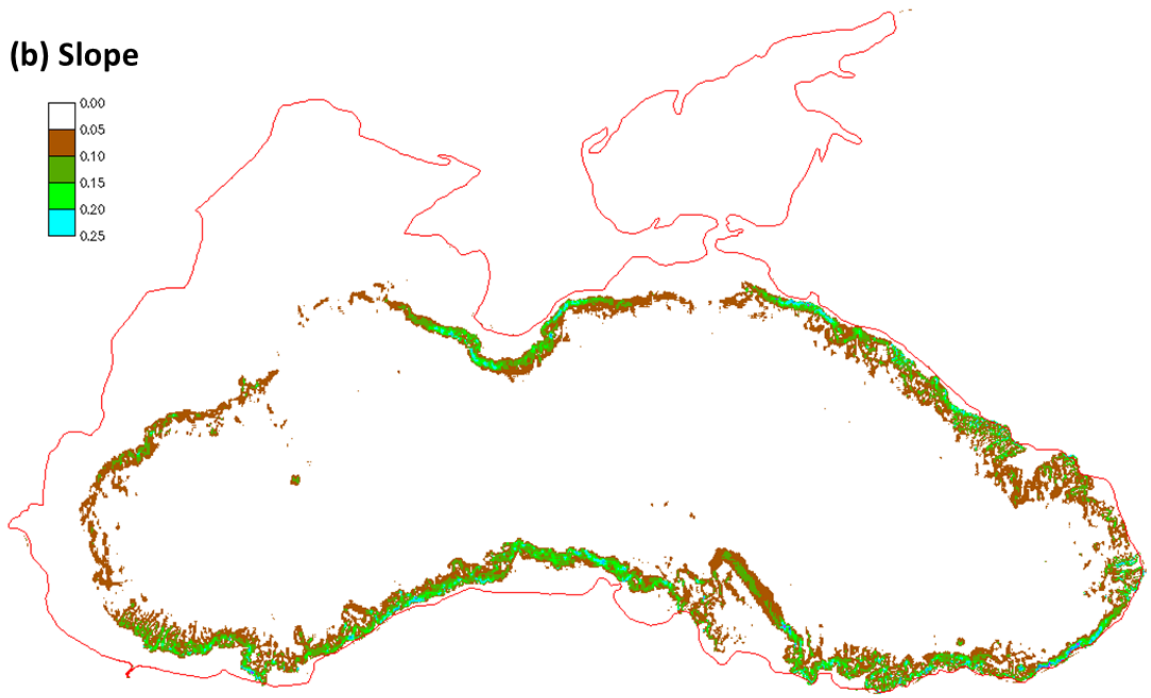
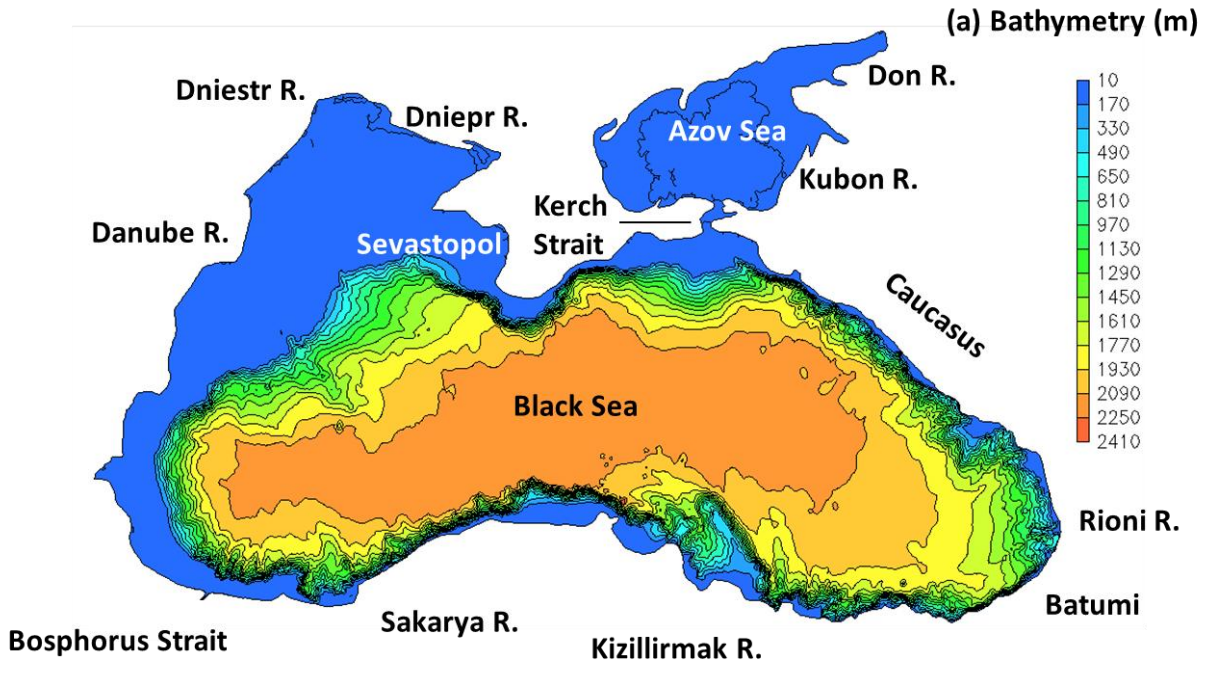
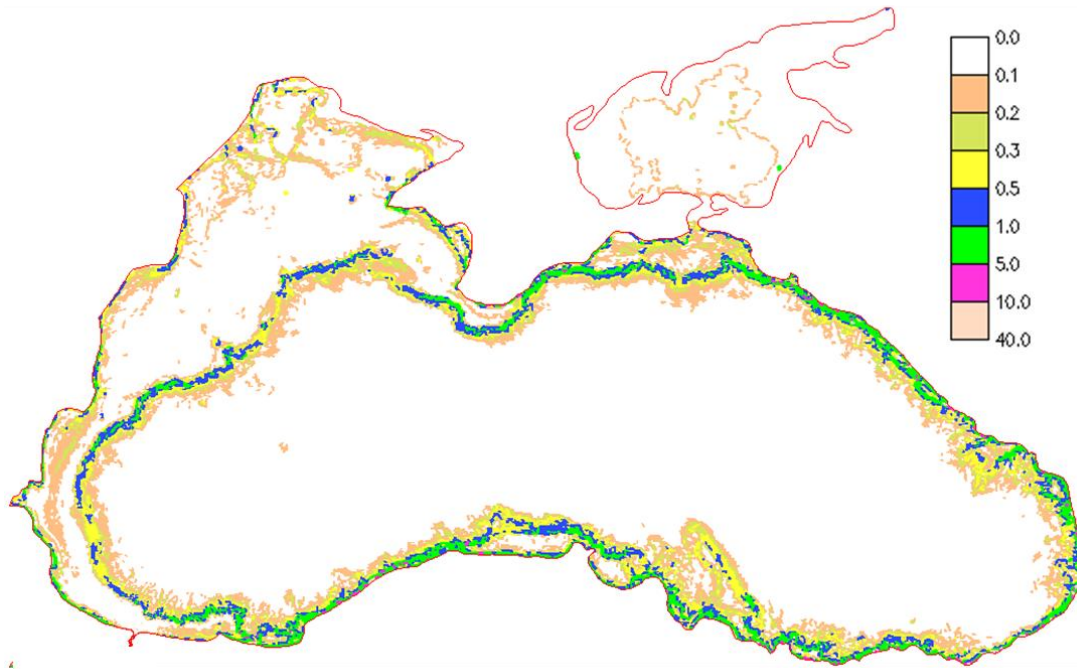


Fig. 14: Snapshot of (a) SSH, (b) temperature at 100m depth, and (c) relative vorticity (scaled by local Coriolis parameter) at 100m depth.



(c) Hannah-Wright ratios



(d) Grid

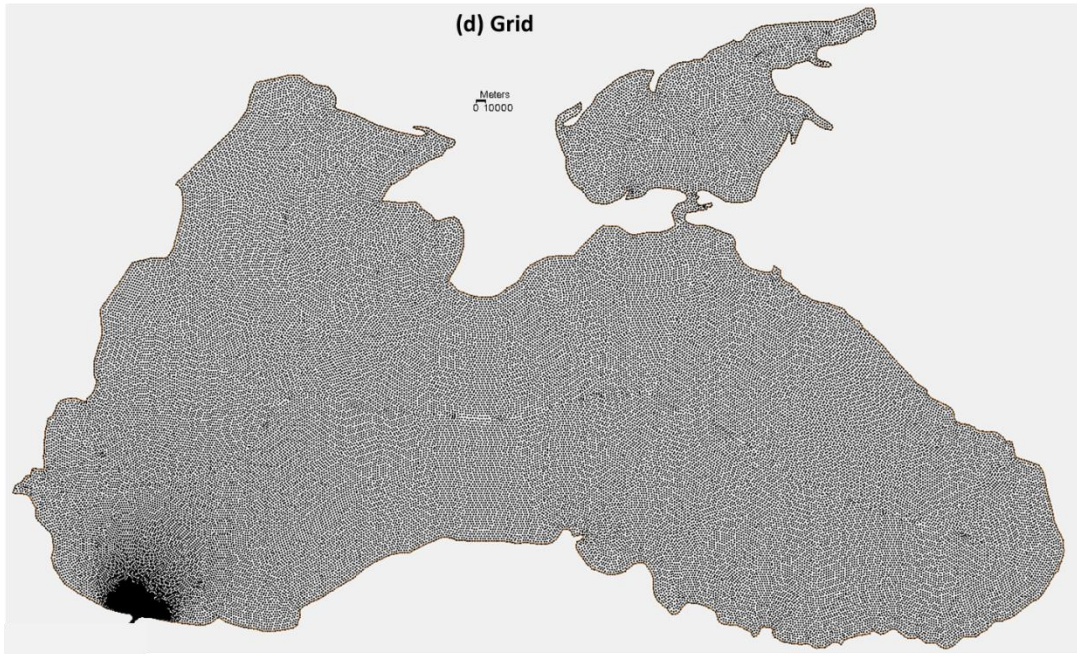
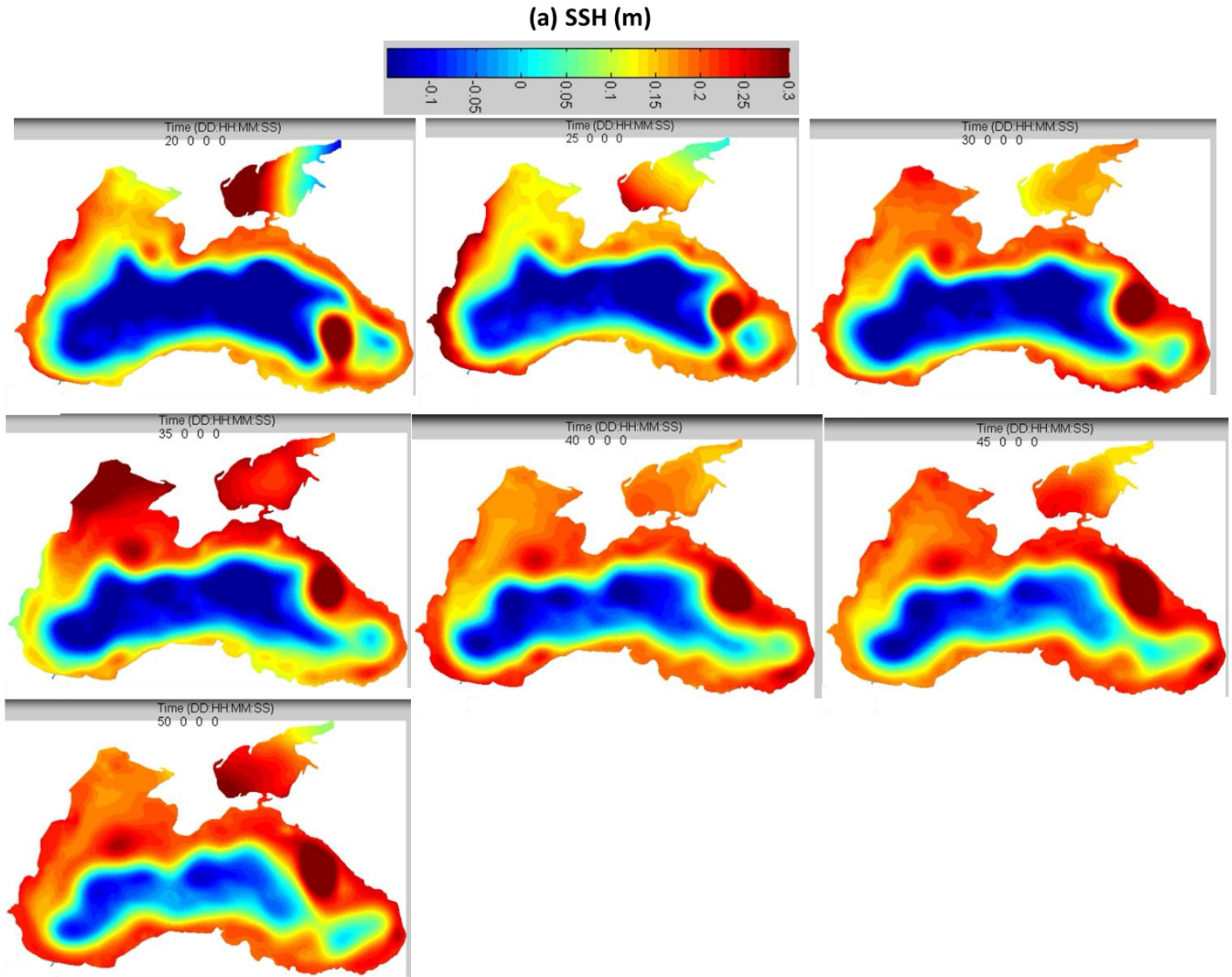


Fig. 15: (a) Black Sea bathymetry. Also shown are major geographic names and rivers around Black Sea (Sakarya, Kizilirmak, Rioni, Dniepr, Dniestr, and Danube) and Azov Sea (Don and Kubon). (b) Bottom slope ($\sqrt{(\partial h/\partial x)^2 + (\partial h/\partial y)^2}$) of Black Sea, with values larger than 0.05 (1:20) being highlighted. (c) Hannah-Wright ratios, with values larger than 0.1 being highlighted. (d) SCHISM grid for Black Sea showing the placement of nodes. Uniform resolution of 3km is used except near the exit to Bosphorus Strait.

Figure16



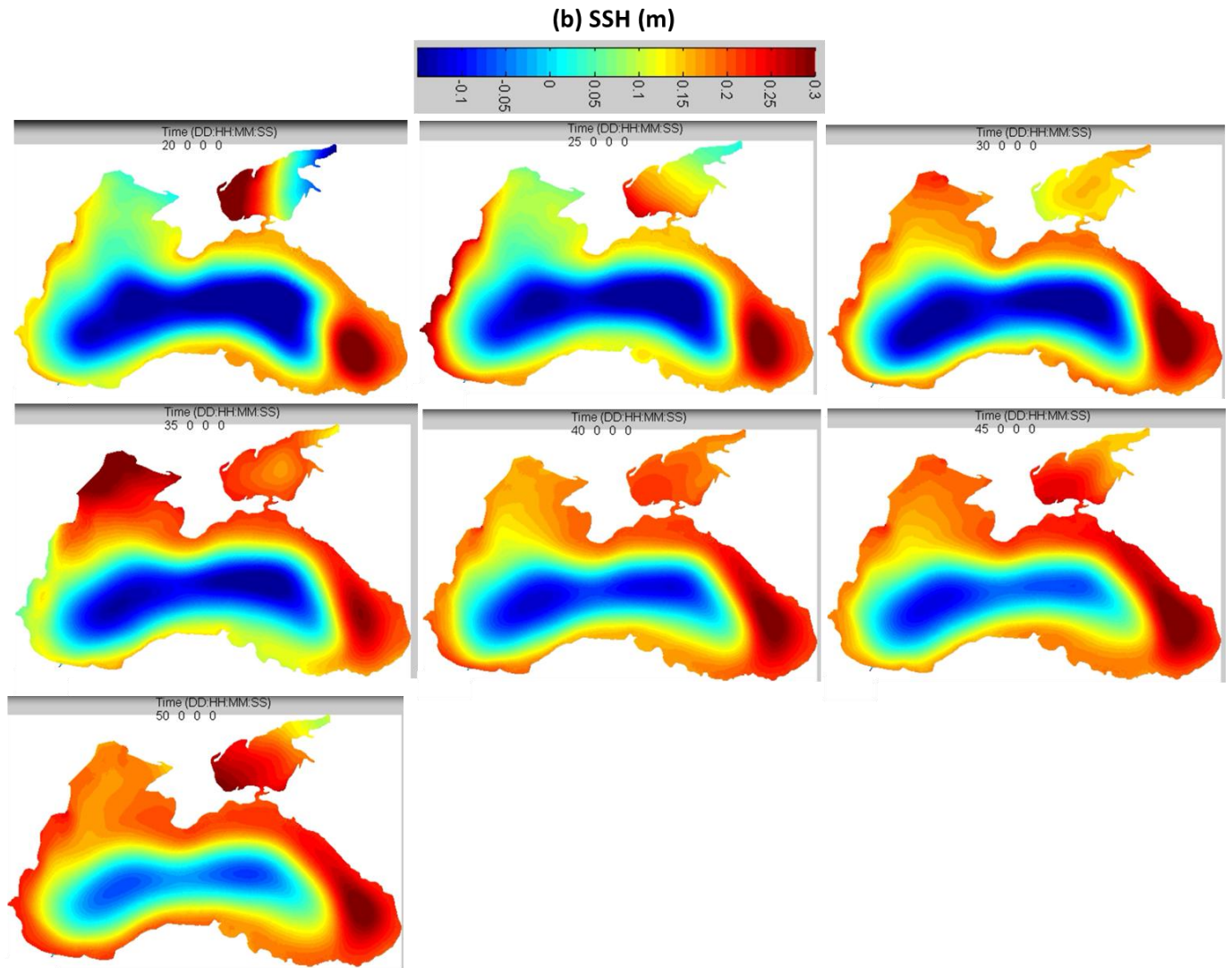


Fig. 16: Snapshots of SSH from (a) SCHISM; (b) SELFE. The time stamps are shown near the top of each panel. Major eddies in Black Sea can be seen in (a) and compared with Stanev (2005).